

Synthesis, Crystal Structure, Thermal Decomposition, and ^{11}B MAS NMR Characterization of $\text{Mg}(\text{BH}_4)_2(\text{NH}_3\text{BH}_3)_2$

Lars H. Jepsen,[†] Voraksmy Ban,[‡] Kasper T. Møller,[†] Young-Su Lee,[§] Young Whan Cho,[§] Flemming Besenbacher,^{||} Yaroslav Filinchuk,[‡] Jørgen Skibsted,[⊥] and Torben R. Jensen^{*,†}

[†]Center for Materials Crystallography, Interdisciplinary Nanoscience Center and Department of Chemistry, Aarhus University, Langelandsgade 140, DK-8000 Aarhus C, Denmark

[‡]Institute of Condensed Matter and Nanosciences, Université catholique de Louvain, Place L. Pasteur 1, B-1348, Louvain-la-Neuve, Belgium

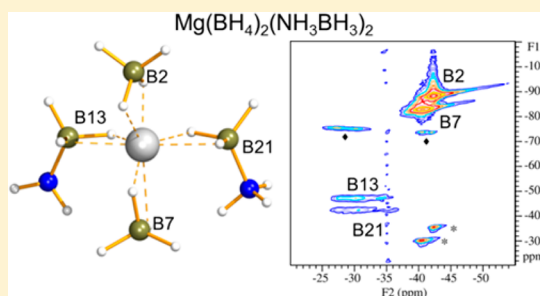
[§]High Temperature Energy Materials Research Center, Korea Institute of Science and Technology, Seoul 136-791, Republic of Korea

^{||}Interdisciplinary Nanoscience Center (iNANO) and Department of Physics and Astronomy, Aarhus University, Ny Munkegade 120, DK-8000 Aarhus C, Denmark

[⊥]Instrument Centre for Solid-State NMR Spectroscopy, Department of Chemistry and Interdisciplinary Nanoscience Center (iNANO), Aarhus University, Langelandsgade 140, DK-8000 Aarhus C, Denmark

Supporting Information

ABSTRACT: A metal borohydride–ammonia borane complex, $\text{Mg}(\text{BH}_4)_2(\text{NH}_3\text{BH}_3)_2$ was synthesized via a solid-state reaction between $\text{Mg}(\text{BH}_4)_2$ and NH_3BH_3 . Different mechanochemical reaction mechanisms are observed, since $\text{Mg}(\text{BH}_4)_2(\text{NH}_3\text{BH}_3)_2$ is obtained from α - $\text{Mg}(\text{BH}_4)_2$, whereas a mixture of $\text{Mg}(\text{BH}_4)_2(\text{NH}_3\text{BH}_3)_2$, NH_3BH_3 , and amorphous $\text{Mg}(\text{BH}_4)_2$ is obtained from γ - $\text{Mg}(\text{BH}_4)_2$. The crystal structure of $\text{Mg}(\text{BH}_4)_2(\text{NH}_3\text{BH}_3)_2$ has been determined by powder X-ray diffraction and optimized by first-principles calculations. The borohydride groups act as terminal ligands, and molecular complexes are linked via strong dihydrogen bonds (<2.0 Å), which may contribute to the high melting point of $\text{Mg}(\text{BH}_4)_2(\text{NH}_3\text{BH}_3)_2$ found to be ~ 48 °C in contrast to those for other molecular metal borohydrides. Precise values for the ^{11}B quadrupole coupling parameters and isotropic chemical shifts are reported for the two NH_3BH_3 sites and two BH_4^- sites in $\text{Mg}(\text{BH}_4)_2(\text{NH}_3\text{BH}_3)_2$ from ^{11}B MAS NMR spectra of the central and satellite transitions and MQMAS NMR. The ^{11}B quadrupole coupling parameters agree excellently with the electric field gradients for the ^{11}B sites from the DFT calculations and suggest that a more detailed structural model is obtained by DFT optimization, which allows evaluation of the dihydrogen bonding scheme.



1. INTRODUCTION

The increasing demand for energy and the environmental problems associated with the use of fossil fuels are the major driving forces for utilization of renewable energy. Hydrogen is recognized as a possible renewable energy carrier since it is widely abundant and environmentally friendly.^{1,2} Complex metal hydrides such as borohydrides and amidoboranes are considered as possible solid-state hydrogen storage materials owing to their high volumetric and gravimetric capacities.^{3–8} However, they typically suffer from poor thermodynamic and/or kinetic properties.

Magnesium borohydride, $\text{Mg}(\text{BH}_4)_2$, is among the most studied borohydrides as a result of its high hydrogen content (14.8 wt % H_2) and complex chemistry. $\text{Mg}(\text{BH}_4)_2$ has been known since the 1950s,⁹ but the crystal structure of the solvent-free polymorph α - $\text{Mg}(\text{BH}_4)_2$ was first reported in 2007.^{10,11} More recently, a new porous polymorph denoted γ - $\text{Mg}(\text{BH}_4)_2$ has been discovered, which can reversibly adsorb small molecules such as H_2 , N_2 , and CH_2Cl_2 .¹² The thermal

decomposition of both α - and γ - $\text{Mg}(\text{BH}_4)_2$ has been intensively studied and turns out to be highly complex.^{13–15} It is reported that α - $\text{Mg}(\text{BH}_4)_2$ transforms into a high-temperature polymorph, β - $\text{Mg}(\text{BH}_4)_2$, at $T \approx 185$ °C, which becomes amorphous at $T \approx 300$ °C before it decomposes.

Another potential hydrogen storage material is ammonia borane, NH_3BH_3 (19.6 wt % H_2 , 146 g H_2/L), which is stable in air.¹⁶ NH_3BH_3 releases one equivalent of hydrogen in each of the three decomposition steps forming polyaminoborane, $[\text{NH}_2\text{BH}_2]_n$ (90–120 °C), polyiminoborane, $[\text{NHBH}]_n$ (120–200 °C), and finally boron nitride, BN (>500 °C).^{17–20} Recently, the regeneration of ammonia borane has been reported to take place from polyiminoborane by reaction with hydrazine in liquid ammonia at 40 °C within 24 h.²¹ However, the hydrogen release is accompanied by volatile and

Received: March 20, 2014

Revised: May 7, 2014

Published: May 8, 2014

Table 1. Composition and Preparation Method for the Investigated Samples

sample	reactants	ratio	molar ratio	preparation method	ρ_m (wt % H ₂)
s1	α -Mg(BH ₄) ₂ -NH ₃ BH ₃	1:1	0.50:0.50	ball milling for 405 min	16.6
s2	α -Mg(BH ₄) ₂ -NH ₃ BH ₃	1:2	0.33:0.67	ball milling for 405 min ^a	17.4
s3	α -Mg(BH ₄) ₂ -NH ₃ BH ₃	1:3	0.25:0.75	ball milling for 405 min	17.9
s4	γ -Mg(BH ₄) ₂ -NH ₃ BH ₃	1:2	0.33:0.67	ball milling for 405 min	17.4
s5	α -Mg(BH ₄) ₂ -NH ₃ BH ₃	1:2	0.33:0.67	manual grinding	17.4
s6	γ -Mg(BH ₄) ₂ -NH ₃ BH ₃	1:0.66	0.60:0.40	compression (pellet)	16.2
s7	γ -Mg(BH ₄) ₂ -NH ₃ BH ₃	1:2	0.33:0.67	compression (pellet)	17.4
s8	amorphous Mg(BH ₄) ₂ -NH ₃ BH ₃	1:2	0.33:0.67	compression (pellet)	17.4

^aFractions of s2 were collected after 100 or 325 min and characterized by PXD.

toxic byproducts, such as ammonia, diborane, and borazine. Metal amidoboranes are a class of materials that prevent the release of the diborane and borazine. They are synthesized by reacting metal hydrides with ammonia borane and typically decompose with fast kinetics and a release of hydrogen below 100 °C.^{22–30} This has prompted further modifications of ammonia borane with use of other complex anions such as amides and borohydrides.^{31–33} Recently, metal borohydrides and ammonia borane were reacted by mechanochemical treatment providing new compounds, i.e., LiBH₄(NH₃BH₃), LiBH₄(NH₃BH₃)_{0.5}, Mg(BH₄)₂(NH₃BH₃)₂, and Ca(BH₄)₂(NH₃BH₃)₂.^{34–36} However, the thermal decomposition of these compounds still involves release of diborane and borazine, like neat NH₃BH₃, reflecting a weak interaction between the borohydride and the ammonia borane. This is also observed in a recent study of NaBH₄-2NH₃BH₃ and KBH₄-2NH₃BH₃ mixtures which are not forming new compounds.³⁷

Physisorption of a small molecular hydride, i.e., ammonia borane, in a porous hydride is a tempting approach, which has motivated the present investigation. Here, we present new synthesis strategies and further structural investigations of the recently described³⁶ Mg(BH₄)₂(NH₃BH₃)₂ complex, using solid-state ¹¹B MAS NMR, synchrotron radiation powder X-ray diffraction data (SR-PXD), and first-principles DFT calculations, which provide new interesting evidence for significant dihydrogen bonding in the borohydride–ammonia borane complex. The thermal decomposition is studied by variable-temperature ¹¹B MAS NMR, in situ SR-PXD, a new photographic setup, and simultaneously thermogravimetric analysis, differential scanning calorimetry, and mass spectroscopy.

2. EXPERIMENTAL SECTION

2.1. Sample Preparation. Ammonia borane, NH₃BH₃ (Sigma-Aldrich, 97%), was used as received. α -Mg(BH₄)₂ was synthesized in-house by reacting dibutyl magnesium, Mg(*n*Bu)₂, with (CH₃)₂S-BH₃ at room temperature, which forms the solvate Mg(BH₄)₂·1/2(CH₃)₂S. Solvent-free α -Mg(BH₄)₂ was obtained by heating the solvate to 140 °C for 3 h in argon atmosphere and followed by vacuum pumping for 1 h.³⁸ The porous polymorph, γ -Mg(BH₄)₂, was prepared by heating the solvate to 80 °C under vacuum for 12 h.¹² The synthesis products were examined by Fourier transform infrared spectroscopy (FTIR) and PXD.

Mixtures of Mg(BH₄)₂-NH₃BH₃ were prepared by ball milling (BM) in the ratios α -Mg(BH₄)₂-NH₃BH₃ (1:1), (1:2), and (1:3) and γ -Mg(BH₄)₂-NH₃BH₃ (1:2), using a Fritsh Pulverisette no. 4. These samples are denoted s1, s2, s3, and s4, respectively, see Table 1. The powders were packed in an inert atmosphere in a tungsten carbide vial (80 mL) together with

tungsten carbide balls (diameter: 10 mm) in the w/w ratio 1:30. The powders were ball milled for 3 min followed by a 3 min break at 400 rpm and this sequence was repeated 135 times (405 min). Fractions of α -Mg(BH₄)₂-NH₃BH₃ (1:2) were collected after 100 and 325 min and characterized by PXD.

A mixture of α -Mg(BH₄)₂ and NH₃BH₃ was also prepared in the molar ratio α -Mg(BH₄)₂-NH₃BH₃ (1:2) by grinding by hand for 3 min in a mortar (sample denoted s5). Moreover, mixtures of γ -Mg(BH₄)₂-NH₃BH₃ (1:0.66) and (1:2) were ground in a similar manner for 10 min, and these samples are denoted s6 and s7, respectively. Samples s6 and s7 were loaded to a pellet die (diameter = 4 mm) followed by compression of the mixtures two times at 0.4 GPa with use of a PerkinElmer Press. The same procedure was repeated for amorphous Mg(BH₄)₂ reacted with NH₃BH₃ in the ratio 1:2 (sample denoted s8). The amorphous Mg(BH₄)₂ was obtained from γ -Mg(BH₄)₂, which becomes amorphous over time.

Fractions of Mg(BH₄)₂(NH₃BH₃)₂ (s2), α -Mg(BH₄)₂, and NH₃BH₃ were heated from room temperature to 220 °C and then cooled to room temperature in a steel autoclave in an argon atmosphere. These samples are denoted s2_220, Mg_220, and NH₃BH₃_220, respectively.

Finally, RbBH₄ (Katchem, Prague, Czech Republic, 98%) and CsBH₄ (Katchem, Prague, Czech Republic, 98%) were mixed with NH₃BH₃ in the molar ratio MBH₄-NH₃BH₃ (1:2) (M = Rb, Cs) and exposed to mechanochemical treatment similarly to the procedure described above for the Mg(BH₄)₂-NH₃BH₃ mixtures. The samples were ball milled for 2 min followed by 2 min break and this sequence was repeated 80 times.

2.2. In-house Powder X-ray Diffraction (PXD). PXD patterns of the as-prepared samples were measured in-house on a Rigaku Smart Lab diffractometer, using a Cu source and a parallel beam multilayer mirror (Cu K α ₁ radiation, λ = 1.540593 Å, Cu K α ₂ radiation, λ = 1.544414 Å). Data were collected in the 2θ range 8–60° at 5 deg/min, using a Rigaku D/tex detector. All air-sensitive samples were mounted in a glovebox in 0.5 mm glass capillaries sealed with glue.

2.3. Synchrotron Radiation Powder X-ray Diffraction (SR-PXD). In situ SR-PXD data were collected for s1 at the Swiss-Norwegian-Beamline (SNBL) at ESRF, Grenoble, France with a Pilatus area detector, λ = 0.822568 Å. The sample was packed in a glass capillary (i.d. 0.5 mm) and heated from room temperature to 100 °C (5 deg/min). Additionally, a PXD pattern was obtained at room temperature for s2 with use of the same setup. This data set was used for initial structural analysis. Subsequently, in situ SR-PXD data with higher resolution were collected for s6 at I11 at Diamond, Oxford, England with a MythenII detector, λ = 0.82712 Å. The sample was packed in a

glass capillary (i.d. 0.5 mm) and was heated from room temperature to 88 °C (10 deg/min). Sample compositions obtained by Rietveld refinement of PXD data only included the crystalline fraction of the sample, since an internal X-ray standard was not used.

2.4. Structure Solution and Refinement. The structure of the complex $\text{Mg}(\text{BH}_4)_2(\text{NH}_3\text{BH}_3)_2$ was solved and refined from SR-PXD data measured at Diamond, UK (a detailed description is given in the Supporting Information). The final Rietveld refinement (Figure 1) indicated that the sample contains $\text{Mg}(\text{BH}_4)_2(\text{NH}_3\text{BH}_3)_2$ (86 wt %), $\alpha\text{-Mg}(\text{BH}_4)_2$ (10 wt %), and 4 wt % of NH_3BH_3 .

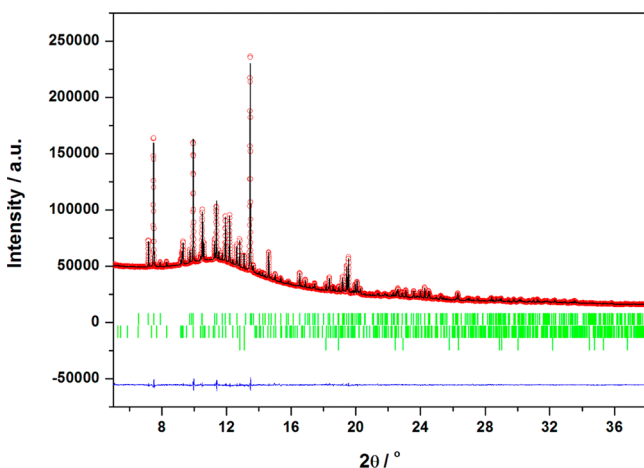


Figure 1. Rietveld refinement of SR-PXD data for $\text{Mg}(\text{BH}_4)_2(\text{NH}_3\text{BH}_3)_2$ measured at room temperature ($\lambda = 0.822568 \text{ \AA}$, sample s6). Tic marks $\alpha\text{-Mg}(\text{BH}_4)_2$ (top), $\text{Mg}(\text{BH}_4)_2(\text{NH}_3\text{BH}_3)_2$ and NH_3BH_3 .

The diffraction data from $\text{Mg}(\text{BH}_4)_2(\text{NH}_3\text{BH}_3)_2$ were indexed with an orthorhombic unit cell, $a = 14.41633(7) \text{ \AA}$, $b = 13.21283(7) \text{ \AA}$, $c = 5.11512(2) \text{ \AA}$, and $V = 974.331(8) \text{ \AA}^3$, using EXPO 2011.³⁹ The structure was solved in the space group $P2_12_12_1$, using global optimization in direct space implemented in the program FOX.⁴⁰ The structural model (Table S1, Supporting Information) was refined by the Rietveld method, using the program Fullprof, and was checked for higher symmetry by using the ADDSYM routine in Platon.^{41,42} The final discrepancy factors are $R_p = 0.66\%$, $R_{wp} = 0.97\%$ (not corrected for background), $R_p = 14.1\%$, $R_{wp} = 8.4\%$ (conventional Rietveld R -factors), $R_{\text{Bragg}} = 6.1\%$, and global $\chi^2 = 28.9$.

2.5. Density Functional Theory Calculation. DFT calculations were performed to further optimize the refined structure from the SR-PXD data. The calculations were carried out by using the Vienna Ab-initio Simulation Package (VASP).⁴³ For the exchange-correlation functional, the generalized-gradient approximation by Perdew, Burke, and Ernzerhof was adopted.⁴⁴ Structural optimization was performed by using VASP projector augmented wave potentials⁴⁵ Mg_{pv} (with semicore p states as valence electrons), B, N, and H until the force on each atom became smaller than 0.005 eV/Å. The plane-wave cutoff energy was set to 500 eV, and a Γ -centered k -point mesh of $2 \times 2 \times 6$ was used. The lattice parameters were fixed to the experimental values since the optimization of the lattice parameters resulted in only 1% increase in volume. For the calculation of the electric field

gradient tensors,⁴⁶ harder potentials Mg_{sv} (with s and p semicore states), B_{h} , N_{h} , and H_{h} , and a higher cutoff energy of 750 eV were used. The atomic positions were not reoptimized.

2.6. Thermal Analysis and Mass Spectroscopy. Thermogravimetric analysis (TGA) was measured for s2 by using a PerkinElmer STA 6000 apparatus simultaneously with mass spectroscopy (MS) analysis of the residual gas with use of a Hiden Analytical HPR-20 QMS sampling system. The samples (approximately 2 mg) were placed in an Al_2O_3 crucible and heated from 40 to 500 °C (2 deg/min) in an argon flow of 65 mL/min. The released gas was analyzed for hydrogen, ammonia, diborane, and borazine. Additionally, thermogravimetric analysis/differential scanning calorimetry (DSC) measurements were performed on s7 with Mettler Toledo instruments, TGA/sDTA 851e and DSC 821, and the heating rate of 5 deg/min from 25 to 500 °C. The samples for the TGA and DSC analysis were loaded in an argon glovebox into alumina crucibles with caps or sealed into aluminum pans, respectively. The experiments were performed with 10 mL/min nitrogen flow to prevent the oxidizing reactions.

2.7. Fourier Transform Infrared Spectroscopy (FTIR). $\alpha\text{-Mg}(\text{BH}_4)_2$, NH_3BH_3 , s2, and the samples heat treated to 220 °C were characterized by infrared absorption spectroscopy by using a NICOLET 380 FT-IR from Thermo Electron Corporation. The samples were exposed to air for approximately 15 s when transferring from the sample vial to the instrument.

2.8. Temperature-Programmed Photographic Analysis. Approximately 10 mg of $\text{Mg}(\text{BH}_4)_2(\text{NH}_3\text{BH}_3)_2$ (s2) and NH_3BH_3 were sealed under argon in a glass tube placed in a home-built aluminum heating block as described recently.⁴⁷ The samples were heated from 25 to 200 °C (heating rate 3 deg/min), while photos of the sample were collected every fifth second.

2.9. ^{11}B NMR Measurements. Solid-state ^{11}B MAS and multiple-quantum (MQ) MAS NMR experiments were performed on a Varian INOVA-300 spectrometer (7.05 T) with use of a home-built variable-temperature (VT) CP/MAS probe for 7 mm o.d. rotors and a home-built CP/MAS NMR probe for 5 mm o.d. rotors. The sample temperature in the NMR rotors was lowered by regulating the temperature of the air-bearing gas with an XRII851D00 Air-Jet sample cooling/heating system (FTS Systems, Stone Ridge, NY). The temperature gradient across the sample is less than 2 and 1 °C for the 7 and 5 mm PSZ rotors, respectively, and the actual sample temperatures were calibrated by using ^{27}Pb MAS NMR of an external sample of $\text{Pb}(\text{NO}_3)_2$ under identical experimental conditions. Dry air (dew point below $-60 \text{ }^\circ\text{C}$) was used for the air-bearing and drive gases in all experiments. The VT ^{11}B MAS NMR spectra following the decomposition of $\text{Mg}(\text{BH}_4)_2(\text{NH}_3\text{BH}_3)_2$ were performed in situ, employing the 7 mm VT CP/MAS probe and a torlon end-cap with a small cylindrical hole (0.8 mm) throughout its center to allow release of gases during the gradual heating of the sample. The experiments used a ^{11}B rf field strength of $\gamma B_1/2\pi = 40 \text{ kHz}$, ^1H TPPM decoupling ($\gamma B_2/2\pi = 50 \text{ kHz}$), a short excitation pulse ($\tau_p = 0.5 \mu\text{s}$), a relaxation delay of 4.0 s, and 256 scans for each spectrum. The ^{11}B MAS NMR spectra of the central and satellite transitions and the ^{11}B MQMAS NMR spectra were acquired at a sample temperature of roughly 31 °C, using the 5 mm CP/MAS probe with the stronger rf field strengths of $\gamma B_1/2\pi = 62 \text{ kHz}$ and $\gamma B_2/2\pi = 70 \text{ kHz}$ for ^{11}B and ^1H , respectively.

The MQMAS spectrum was obtained with the three-pulse, z -filter sequence,⁴⁸ employing TPPM ^1H decoupling during both the t_1 evolution and t_2 detection periods. A few ^{11}B MAS NMR spectra were acquired at 14.09 T, using a home-built CP/MAS probe for 4 mm rotors, spinning speeds of $\nu_{\text{R}} = 10.0\text{--}12.0$ kHz, and a $0.5\ \mu\text{s}$ excitation pulse for an rf field strength of $\gamma B_1/2\pi = 60$ kHz. The determination of the ^{11}B quadrupole coupling parameters (C_{Q} and η_{Q}) and isotropic chemical shifts (δ_{iso}) was performed by least-squares fitting of simulated to experimental spectra for either the central transition or satellite transitions, using the STARS software package.⁴⁹ The ^{11}B isotropic chemical shifts are in ppm relative to neat $\text{F}_3\text{B}\cdot\text{O}(\text{CH}_2\text{CH}_3)_2$.

3. RESULTS AND DISCUSSION

3.1. Synthesis of $\text{Mg}(\text{BH}_4)_2(\text{NH}_3\text{BH}_3)_2$ from $\alpha\text{-Mg}(\text{BH}_4)_2$ -PXD patterns (Figure 2) have been collected for $\alpha\text{-Mg}(\text{BH}_4)_2$ -

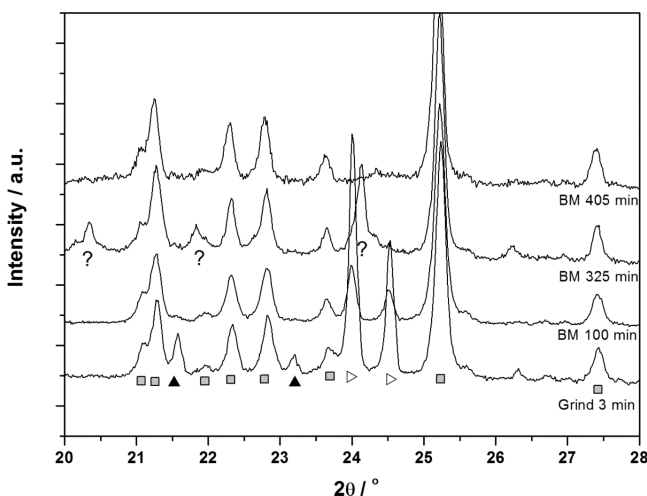
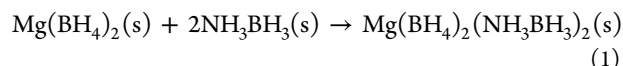


Figure 2. PXD patterns of $\alpha\text{-Mg}(\text{BH}_4)_2\text{-NH}_3\text{BH}_3$ (1:2) collected after 3 min of grinding (s5) and after various ball milling times (s2) showing the progress of the synthesis of $\text{Mg}(\text{BH}_4)_2(\text{NH}_3\text{BH}_3)_2$ ($\lambda = 1.54056$ Å). Symbols: \triangleright , NH_3BH_3 ; \blacktriangle , $\alpha\text{-Mg}(\text{BH}_4)_2$; (filled gray square), $\text{Mg}(\text{BH}_4)_2(\text{NH}_3\text{BH}_3)_2$; $?$, 1.

NH_3BH_3 (1:2, s5) after 3 min of manual grinding and for $\alpha\text{-Mg}(\text{BH}_4)_2\text{-NH}_3\text{BH}_3$ (1:2, s2) after different BM times. The PXD patterns show reflections from the newly produced compound, $\text{Mg}(\text{BH}_4)_2(\text{NH}_3\text{BH}_3)_2$ complex, and the unreacted starting materials, $\alpha\text{-Mg}(\text{BH}_4)_2$ and NH_3BH_3 , for the s5 mixture after 3 min of manual grinding, demonstrating that a mechanochemical reaction readily takes place. After ball milling for 100 min the intensity of the reflections from NH_3BH_3 decreases, and after 325 min all reflections from $\text{Mg}(\text{BH}_4)_2$ and NH_3BH_3 have disappeared. Thus, only reflections from $\text{Mg}(\text{BH}_4)_2(\text{NH}_3\text{BH}_3)_2$ and a new set of unidentified reflections, denoted 1 ($d = 6.890, 6.595, 5.075, 4.793, 4.712, 4.393, 4.352, 4.059, 3.678, 3.622, 3.889, 3.000, 2.553, \text{ and } 2.538$ Å) are observed after mechanochemical treatment for 325 min. The reflections listed above may originate from another new compound, 1, in the system $\text{Mg}(\text{BH}_4)_2\text{-NH}_3\text{BH}_3$, which may be formed in a side reaction. The sample was stored at room temperature for 5 days before a SR-PXD pattern was collected (Figure S1, Supporting Information), which also includes a few new unidentified reflections, denoted 2 ($d = 6.617, 5.734, 5.093, 4.479, 4.332, \text{ and } 3.180$ Å). The change in d -values for the unidentified reflections may reflect transformation from one unstable compound to another in the $\text{Mg}(\text{BH}_4)_2\text{-NH}_3\text{BH}_3$

system. A Rietveld refinement has been performed for compound 2 with the crystal structure of $\gamma\text{-Mg}(\text{BH}_4)_2$. There are significant shifts in the cell parameters for 2 ($a = 16.2234$ Å) as compared to $\gamma\text{-Mg}(\text{BH}_4)_2$ ($a = 15.7575$ Å), which may reflect that NH_3BH_3 is physisorbed in the porous structures of $\gamma\text{-Mg}(\text{BH}_4)_2$. However, when a guest molecule is adsorbed in the pores, the relative intensity between the peaks for $\gamma\text{-Mg}(\text{BH}_4)_2$ normally changes, which is not observed for the data obtained for 2.¹² After 405 min of BM all reflections can be assigned to $\text{Mg}(\text{BH}_4)_2(\text{NH}_3\text{BH}_3)_2$, reflecting a completed reaction according to reaction 1.



Ball milling of the $\text{Mg}(\text{BH}_4)_2\text{-NH}_3\text{BH}_3$ (1:1) and (1:3) mixtures also produces $\text{Mg}(\text{BH}_4)_2(\text{NH}_3\text{BH}_3)_2$, however, with an excess of either $\text{Mg}(\text{BH}_4)_2$ or NH_3BH_3 . This is in contrast to the $\text{LiBH}_4\text{-NH}_3\text{BH}_3$ system, where either $\text{LiBH}_4(\text{NH}_3\text{BH}_3)$ or $\text{LiBH}_4(\text{NH}_3\text{BH}_3)_{0.5}$ has been synthesized by ball milling depending on the ratio of LiBH_4 and NH_3BH_3 .³⁵ $\text{Mg}(\text{BH}_4)_2(\text{NH}_3\text{BH}_3)_2$ transforms into a foam when it is stored at room temperature for several weeks (Figure S2, Supporting Information). Therefore, all samples containing $\text{Mg}(\text{BH}_4)_2(\text{NH}_3\text{BH}_3)_2$ have been stored at -35 °C.

3.2. Synthesis of $\text{Mg}(\text{BH}_4)_2(\text{NH}_3\text{BH}_3)_2$ from Porous $\gamma\text{-Mg}(\text{BH}_4)_2$. The synthesis of $\text{Mg}(\text{BH}_4)_2(\text{NH}_3\text{BH}_3)_2$ by using the porous $\gamma\text{-Mg}(\text{BH}_4)_2$ polymorph rather than $\alpha\text{-Mg}(\text{BH}_4)_2$ as starting material has also been investigated. This work was prompted by the idea of adsorption of NH_3BH_3 in the porous structure. After manual grinding of $\gamma\text{-Mg}(\text{BH}_4)_2\text{-NH}_3\text{BH}_3$ (1:0.66, s6) for 10 min, 50 wt % conversion into the complex $\text{Mg}(\text{BH}_4)_2(\text{NH}_3\text{BH}_3)_2$ is obtained (Figure S3, Supporting Information). After compressing the ground sample two times at 0.4 GPa, the resulting pellet contained more than 85 wt % of $\text{Mg}(\text{BH}_4)_2(\text{NH}_3\text{BH}_3)_2$ and ~ 12 wt % of NH_3BH_3 based on the detected content of crystalline components only (Figure S4, Supporting Information). Compression (0.4 GPa) of $\gamma\text{-Mg}(\text{BH}_4)_2\text{-NH}_3\text{BH}_3$ (1:2, s7) also produces $\text{Mg}(\text{BH}_4)_2(\text{NH}_3\text{BH}_3)_2$, but with a larger excess of NH_3BH_3 . The compressed samples also contain varying amounts of amorphous $\gamma\text{-Mg}(\text{BH}_4)_2$, observed as a broad hump in the PXD background centered at $\sim 8\text{--}12$ °. A mechanochemically treated sample of $\gamma\text{-Mg}(\text{BH}_4)_2\text{-NH}_3\text{BH}_3$ (1:2, s4) reveals crystalline $\text{Mg}(\text{BH}_4)_2(\text{NH}_3\text{BH}_3)_2$ (95 wt %) and unreacted NH_3BH_3 (5 wt %), as obtained by Rietveld refinement (Figure S5, Supporting Information). The solid-state ^{11}B MAS NMR spectrum of this sample (Figure S6, Supporting Information) is dominated by the resonances from $\text{Mg}(\text{BH}_4)_2(\text{NH}_3\text{BH}_3)_2$; however, resonances from unreacted NH_3BH_3 and amorphous $\text{Mg}(\text{BH}_4)_2$ have also been identified although they overlap with the peaks from the BH_3 and BH_4^- sites of the $\text{Mg}(\text{BH}_4)_2(\text{NH}_3\text{BH}_3)_2$ complex, respectively. This indicates that amorphous $\gamma\text{-Mg}(\text{BH}_4)_2$ does not react with NH_3BH_3 . This hypothesis is verified by reacting amorphous $\text{Mg}(\text{BH}_4)_2$ with NH_3BH_3 (s8), which surprisingly does not result in any formation of $\text{Mg}(\text{BH}_4)_2(\text{NH}_3\text{BH}_3)_2$ as seen by Figure S7 (Supporting Information). This is a rare observation of different reactivity for the two polymorphs, $\gamma\text{-Mg}(\text{BH}_4)_2$ and $\alpha\text{-Mg}(\text{BH}_4)_2$. Thus, synthesis of $\text{Mg}(\text{BH}_4)_2(\text{NH}_3\text{BH}_3)_2$ from $\gamma\text{-Mg}(\text{BH}_4)_2$ appears not to be well reproducible as a result of a partial amorphization of the porous reactant.

To further investigate the unidentified compounds, 1 and 2, observed during synthesis from $\alpha\text{-Mg}(\text{BH}_4)_2$ and in an attempt

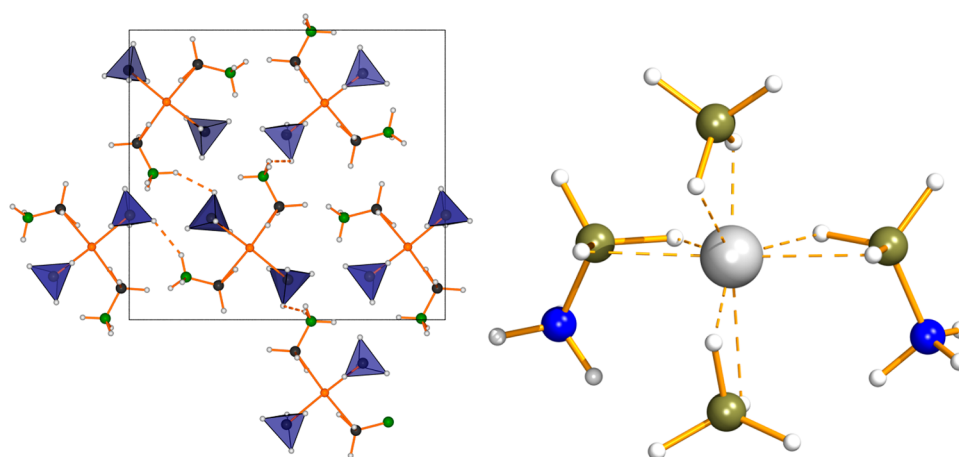


Figure 3. Left: Crystal structure of $\text{Mg}(\text{BH}_4)_2(\text{NH}_3\text{BH}_3)_2$ identified by X-ray powder diffraction. Molecular complexes of $[\text{Mg}(\text{BH}_4)_2(\text{NH}_3\text{BH}_3)_2]$ are connected by dihydrogen bonds (dotted lines). Right: The neutral mononuclear $[\text{Mg}(\text{BH}_4)_2(\text{BH}_3\text{NH}_3)_2]$ complex. Mg, B, N, and H are represented by gray, green, blue, and white spheres, respectively.

to adsorb NH_3BH_3 in the pores of $\gamma\text{-Mg}(\text{BH}_4)_2$, the ball milling process has been characterized by in situ SR-PXD (see the Supporting Information). However, under the applied physical conditions, **1** and **2** have not been observed (Figures S8 and S9, Supporting Information), and there are no signs of adsorption of NH_3BH_3 in $\gamma\text{-Mg}(\text{BH}_4)_2$ (Figures S12 and S13, Supporting Information).

3.3. Crystal Structure of $\text{Mg}(\text{BH}_4)_2(\text{NH}_3\text{BH}_3)_2$. The structure of $\text{Mg}(\text{BH}_4)_2(\text{NH}_3\text{BH}_3)_2$ contains two independent borohydride groups and two NH_3BH_3 molecules coordinated via BH_2 edges to the same Mg atom. This way the BH_4^- anions and the NH_3BH_3 molecules act as terminal η^2 -ligands. The resulting structure contains mononuclear neutral molecular complexes, shown in Figure 3. The molecule is taking a general position with multiplicity 4, but displays a pseudosymmetry with a mirror plane passing through the Mg atom and the BH_4^- anions (corresponds to $[110]$ and $[1\bar{1}0]$ directions).

The Mg^{2+} cation has a distorted tetrahedral coordination, with B–Mg–B angles ranging from $97.0(2)^\circ$ to $134.1(2)^\circ$, similar to the range $92.1(1)–129.0(1)^\circ$ found for $\alpha\text{-Mg}(\text{BH}_4)_2$ ⁵⁰ and $100.4–129.6^\circ$ found in $\gamma\text{-Mg}(\text{BH}_4)_2$.¹² The MgH_8 coordination polyhedron corresponds to a J84 Johnson solid, also known as a snub disphenoid. The same geometry of this coordination polyhedron has been observed in α - and γ - $\text{Mg}(\text{BH}_4)_2$ and is assumed to be important for the stability of these most common polymorphs. The Mg–H distances are not symmetrical, showing a span from 1.75 to 2.33 Å; however, this may be due to the low X-ray scattering power of H. The Mg–B distances involving the borohydride groups are slightly shorter than those for the BH_3 groups in NH_3BH_3 and are equal to 2.41 and 2.48 Å. The Mg–B–N angles are $120.1(4)^\circ$ and $114.0(4)^\circ$. The molecular complexes are linked in the crystal structure via dihydrogen bonds of the type $\text{N–H}^{\delta+}\cdots\delta^-\text{H–B}$. The main geometrical parameters for the four strongest $\text{H}\cdots\text{H}$ bonds are listed in Table S2 (Supporting Information). Only one contact is shorter than 2.0 Å. As expected, the N–H \cdots H angles are more open for the shorter $\text{H}\cdots\text{H}$ bonds, while the B–H \cdots H angles show a large spread.⁵¹

The DFT optimization starting from the refined PXD structure suggests only minor changes to the structure, confirming the structural model. The optimized Mg–H distances become more homogeneous, distributed between 1.971 and 2.074 Å. In accordance with the experimental

structure, borohydride groups approach closer to Mg than the NH_3BH_3 groups. Thus, average Mg–B and Mg–H distances are 2.394 and 1.996 Å for BH_4^- , and 2.469 and 2.064 Å for NH_3BH_3 . An overview with selected bond lengths and fractional atomic coordinates from the DFT-optimized structure are given in Tables S3 and S4 (Supporting Information), respectively. The B–H bonds that coordinate Mg are more stretched by 0.02 Å on average than the other B–H bonds for both BH_4^- and NH_3BH_3 .

The DFT-optimized H positions reveal a stronger dihydrogen bonding network than what is expected from the experimental structure. We note that the short dihydrogen bondings always appear intermolecular and form across different molecular complexes, and not between BH_4^- and NH_3BH_3 within the same complex. Each neutral molecular complex $[\text{Mg}(\text{BH}_4)_2(\text{NH}_3\text{BH}_3)_2]$ is linked to the neighboring ones via four strong $\text{H}\cdots\text{H}$ bonds shorter than 2.0 Å (symmetrically equivalent pairs with distances of 1.957 and 1.995 Å). When the cutoff distance is increased to 2.1 Å, the number of short bondings increases from four to ten. This is in contrast to a previous study where the stronger dihydrogen bonds were observed within one complex between adjacent BH_4^- and NH_3BH_3 (2.21 to 2.27 Å) and the weaker between neighboring complexes (2.24 to 2.39 Å).³⁶ This is the main difference between the structure solutions presented here and in a previous study.³⁶ In the earlier investigation the unit cell parameters are reported to be $a = 14.4135(2)$ Å, $b = 13.2084(2)$ Å, and $c = 5.1118(1)$ Å, while $a = 14.41633(7)$ Å, $b = 13.21283(7)$ Å, and $c = 5.11512(2)$ Å are determined in this work.

The mononuclear molecular structure of $\text{Mg}(\text{BH}_4)_2(\text{NH}_3\text{BH}_3)_2$ resembles those of $\text{Al}(\text{BH}_4)_3$ and $\text{Zr}(\text{BH}_4)_4$,^{52–54} where the borohydride groups act as terminal ligands. However, the borohydride groups share a face (η^3 -coordination) for $\text{Zr}(\text{BH}_4)_4$ and an edge with Mg (η^2) in $\text{Mg}(\text{BH}_4)_2(\text{NH}_3\text{BH}_3)_2$. The three other metal borohydride complexes with NH_3BH_3 , known so far, show strikingly different connectivities, where the BH_4^- groups and the NH_3BH_3 molecules act as bridging ligands. In $\text{Ca}(\text{BH}_4)_2(\text{NH}_3\text{BH}_3)_2$,³⁴ the borohydride groups are bridging two metal atoms, forming a 2D square net. The NH_3BH_3 molecules behave as terminal ligands, completing the coordination sphere of Ca to octahedral. In

$\text{LiBH}_4(\text{NH}_3\text{BH}_3)_{0.5}$,³⁴ the borohydride groups are bridging three metal atoms and the NH_3BH_3 molecules are coordinated by two metal atoms, making a 3D polymeric framework. The $\text{LiBH}_4(\text{NH}_3\text{BH}_3)_2$ structure appears to be very complex,³⁵ containing four independent borohydride anions and four NH_3BH_3 molecules. While the borohydride anions are coordinated to 2–4 metal atoms, the NH_3BH_3 molecules act as a terminal ligand or even stay isolated from metal atoms, forming a cocrystal. Thus, $\text{Mg}(\text{BH}_4)_2(\text{BH}_3\text{NH}_3)_2$ is the only known molecular complex of ammonia borane, having a potential to show a relatively high vapor pressure at temperatures close to ambient.

3.4. ^{11}B MAS and MQMAS NMR of $\text{Mg}(\text{BH}_4)_2(\text{NH}_3\text{BH}_3)_2$. The ^{11}B MAS NMR spectrum of the central transition region for $\text{Mg}(\text{BH}_4)_2(\text{NH}_3\text{BH}_3)_2$ (Figure 4a, sample s2) clearly reveals

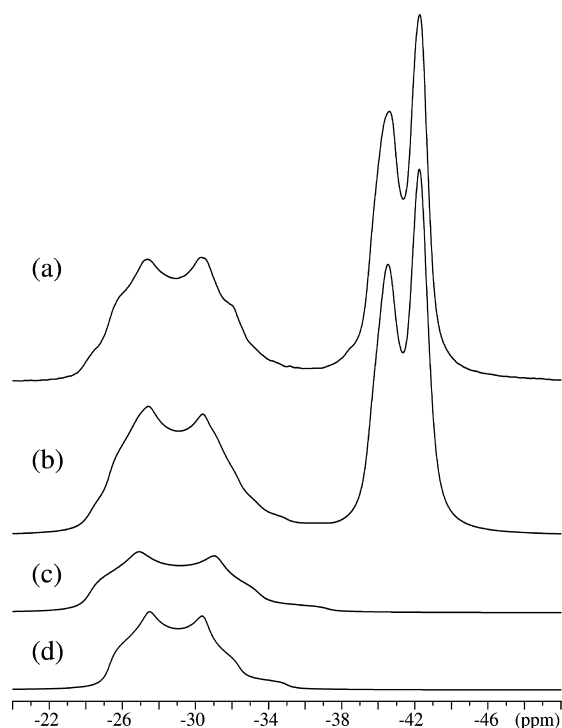


Figure 4. (a) ^{11}B MAS NMR spectrum (7.05 T, $\nu_R = 9.0$ kHz) of the central transitions for $\text{Mg}(\text{BH}_4)_2(\text{NH}_3\text{BH}_3)_2$ (s2), obtained at a sample temperature of 31 °C. (b) Optimized simulated spectrum for the central transitions, employing the δ_{iso} , C_Q , and η_Q parameters listed in Table 2. Parts c and d illustrate simulated second-order quadrupolar line shapes for the B(13)– NH_3BH_3 and B(21)– NH_3BH_3 sites, respectively, as obtained from least-squares fitting to the spectrum in part a.

the presence of two distinct BH_4^- sites, as observed by the narrow resonances at -40 and -42 ppm. Moreover, center-band resonances exhibiting second-order quadrupolar line shapes are observed in the range -24 to -34 ppm. These line shapes are removed in the isotropic (F1) dimension of the MQMAS NMR spectrum (Figure 5), which unambiguously shows the presence of two distinct sites in the -24 to -34 ppm spectral region. Thus, this region is analyzed by spectral simulations/optimizations by using two overlapping quadrupolar line shapes, assigned to the two distinct NH_3BH_3 sites. This results in the optimized ^{11}B isotropic chemical shifts (δ_{iso}) and quadrupole coupling parameters (C_Q and η_Q) listed in Table 2 and illustrated by the simulations in Figure 4c,d.

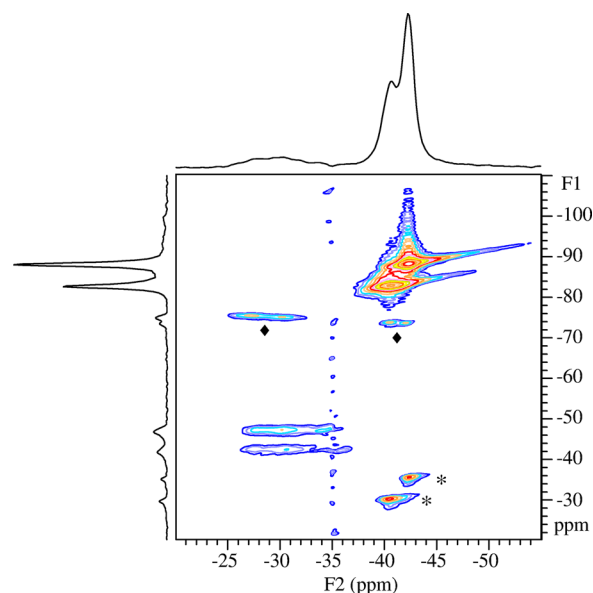


Figure 5. ^{11}B MQMAS NMR spectrum (7.05 T, $\nu_R = 9.0$ kHz) of $\text{Mg}(\text{BH}_4)_2(\text{NH}_3\text{BH}_3)_2$ (s2), obtained at a sample temperature of 31 °C using the three-pulse z-filter sequence, 192 t_1 increments, a 3.5 s relaxation delay, 72 scans for each increment, and ^1H decoupling during both the t_1 and t_2 periods. The projections onto the F1 and F2 axes represent summations over the 2D spectrum. The asterisks indicate spinning sidebands for the two BH_4^- sites and the diamonds indicate artifacts arising around the transmitter frequency in the F1 dimension.

Accurate values for δ_{iso} , C_Q and η_Q cannot be obtained by line shape analysis of the central transitions for the two BH_4^- sites since these display Gaussian-like line shapes. However, two distinct manifolds of spinning sidebands (ssb's) from the satellite transitions are observed for the two BH_4^- sites, as illustrated in Figure 6a. Least-squares analyses to the intensities and partly overlapping line shapes for the two manifolds allow determination of the quadrupole interaction parameters with high precision (Table 2). This is also apparent from the simulation spectrum of the ssb manifolds for the two BH_4^- sites only in Figure 6b, which matches very well the experimental intensities and line shapes. The high precision of the δ_{iso} , C_Q and η_Q parameters determined for the two NH_3BH_3 sites and two BH_4^- sites are further supported by the isotropic triple-quantum shifts (δ_{3Q}^{exp} , Table 2) observed in the ^{11}B MQMAS NMR spectrum (Figure 5). These shifts depends on the δ_{iso} , C_Q and η_Q parameters, following the relationship

$$\delta_{3Q}^{\text{calc}} = \frac{17}{8} \delta_{\text{iso}} + \frac{1}{32} \frac{C_Q^2 (1 + \eta_Q^2/3)}{\nu_L^2} \times 10^6 \quad (2)$$

The calculated values ($\delta_{3Q}^{\text{calc}}$), using the parameters determined from the ^{11}B MAS NMR spectra (Figures 4 and 6) and listed in Table 2, match fully the experimental values within their error limits. Finally, Figure 4b illustrates a full simulation of the central transition region, using the ^{11}B NMR parameters in Table 2 and relative intensities for the individual sites in the range 0.90–1.05. In the ^{11}B MQMAS spectrum, the intensities for the NH_3BH_3 sites are significantly smaller than those for the two BH_4^- sites, which reflect the reduced efficiency of triple-quantum (3Q) excitation and triple-quantum to single-quantum conversion for ^{11}B sites with large quadrupole couplings.

Table 2. ^{11}B Quadrupole Coupling Parameters (C_Q , η_Q), Isotropic Chemical Shifts (δ_{iso}), and Triple-Quantum Chemical Shifts (δ_{3Q}) Determined for $\text{Mg}(\text{BH}_4)_2(\text{BH}_3\text{NH}_3)_2$ at 31°C^a

site ^b	δ_{iso} (ppm)	C_Q (MHz)	η_Q	δ_{3Q}^{exp} (ppm)	$\delta_{3Q}^{\text{calc}}$ (ppm) ^c
B(2)– BH_4^-	-41.8 ± 0.1	0.409 ± 0.020	0.71 ± 0.03	-88.1 ± 0.2	-88.1
B(7)– BH_4^-	-39.5 ± 0.2	0.568 ± 0.020	0.73 ± 0.03	-82.7 ± 0.2	-82.6
B(13)– NH_3BH_3	-23.4 ± 0.3	1.419 ± 0.030	0.35 ± 0.05	-42.5 ± 0.2	-42.6
B(21)– NH_3BH_3	-24.7 ± 0.3	1.221 ± 0.025	0.38 ± 0.02	-47.1 ± 0.2	-47.3

^aThe quadrupole coupling and chemical shift parameters are determined from optimization to spectra of the central transition and the satellite transitions for the NH_3BH_3 and BH_4^- sites, respectively. The quadrupole coupling parameters are $C_Q = eQV_{zz}/h$, $\eta_Q = (V_{yy} - V_{xx})/V_{zz}$, where V_{ii} are the principal elements of the electric field gradient tensor, following the convention: $|V_{zz}| \geq |V_{xx}| \geq |V_{yy}|$. ^bAssignment to the different crystallographic B sites from the SR-PXD structure determination (Table S1, Supporting Information) based on the calculated ^{11}B electric field gradient tensors by DFT in Table 3. ^cThe triple-quantum shifts are calculated from δ_{iso} , C_Q and η_Q using the expression in eq 2.

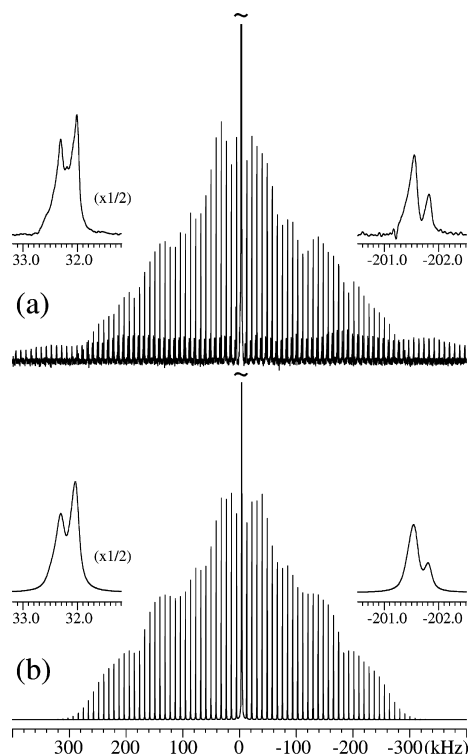


Figure 6. (a) ^{11}B MAS NMR spectrum (7.05 T, $\nu_R = 9.0$ kHz) illustrating the satellite transitions for the two BH_4^- sites in $\text{Mg}(\text{BH}_4)_2(\text{NH}_3\text{BH}_3)_2$ (s2), obtained at a sample temperature of 31°C . (b) Optimized simulated spectrum for the central and satellite transitions for the two BH_4^- sites, employing the δ_{iso} , C_Q and η_Q parameters listed in Table 2. The insets show the partially resolved sidebands for the two BH_4^- sites.

The ^{11}B MAS NMR spectra (Figures 4–6) and parameters (Table 2) reveal the presence of four distinct boron sites in tetrahedral coordination, corresponding to two BH_4^- and two NH_3BH_3 sites, in agreement with the crystal structure for $\text{Mg}(\text{BH}_4)_2(\text{NH}_3\text{BH}_3)_2$. The electric field gradients at the nuclear ^{11}B sites will be more distorted for the NH_3BH_3 sites as compared to the BH_4^- sites, as reflected by the larger quadrupolar couplings for the NH_3BH_3 sites.

The ^{11}B NMR parameters (Table 2) can be assigned to the different BH_4^- and BH_3 sites in the crystal structure of $\text{Mg}(\text{BH}_4)_2(\text{NH}_3\text{BH}_3)_2$ utilizing calculated ^{11}B electric field gradient (EFG) tensor elements (V_{zz}^{calc} , V_{yy}^{calc} , V_{xx}^{calc}) from the DFT calculations and the approach described earlier for experimental and calculated ^{11}B NMR parameters for inorganic borates.⁵⁵ ^{11}B quadrupole coupling tensor elements (Q_{zz}^{exp} , Q_{yy}^{exp} , Q_{xx}^{exp}) are calculated from C_Q and η_Q as

$$\begin{aligned} Q_{zz}^{\text{exp}} &= C_Q \\ Q_{yy}^{\text{exp}} &= -\frac{1}{2}(1 - \eta_Q)C_Q \\ Q_{xx}^{\text{exp}} &= -\frac{1}{2}(1 + \eta_Q)C_Q \end{aligned} \quad (3)$$

The sign of C_Q cannot be determined from single-pulse NMR experiments and thus it is assumed that the experimental C_Q values exhibit the same sign as the corresponding V_{zz}^{calc} elements from the DFT calculations. The calculated ^{11}B EFG's and quadrupole coupling parameters from the DFT calculations before and after a DFT optimization of the structure determined from SR-PXD (Table S1, Supporting Information) are listed in Table 3. Both of these sets of calculated ^{11}B EFG

Table 3. Calculated ^{11}B Quadrupole Coupling Parameters (C_Q^{calc} , η_Q^{calc}) and EFG Tensors Elements (V_{xx}^{calc} , V_{yy}^{calc} , V_{zz}^{calc}) by DFT Calculations before and after DFT Optimization of the PXD Structure for $\text{Mg}(\text{BH}_4)_2(\text{BH}_3\text{NH}_3)_2$

site ^a	C_Q^{calc} (MHz) ^b	η_Q^{calc}	V_{xx}^{calc} ($\text{V}/\text{\AA}^2$)	V_{yy}^{calc} ($\text{V}/\text{\AA}^2$)	V_{zz}^{calc} ($\text{V}/\text{\AA}^2$)
PXD–B(2)	0.54	0.92	-5.695	-0.225	5.920
PXD–B(7)	0.70	0.77	-6.779	-0.899	7.678
PXD–B(13)	1.36	0.72	-12.768	-2.120	14.888
PXD–B(21)	1.34	0.34	-9.797	-4.830	14.627
DFT–B(2)	0.51	0.38	3.826	1.735	-5.561
DFT–B(7)	0.78	0.61	6.815	1.656	-8.470
DFT–B(13)	1.46	0.50	-11.925	-4.026	15.951
DFT–B(21)	1.24	0.40	-8.585	-3.690	12.275

^aIndexes for the B sites according to the SR-PXD structure determination (Table S1, Supporting Information). PXD denotes calculated data for the SR-PXD structure whereas DFT corresponds to the parameters obtained after a DFT structure optimization of the PXD structure. ^bThe calculated quadrupole coupling constants are obtained with the ^{11}B quadrupole moment, $Q = 0.0406 \times 10^{-28} \text{ m}^2$.^{56,57}

tensor elements result in the same assignment of the observed ^{11}B quadrupole coupling parameters (Table 2) to the B(2), B(7), B(13), and B(21) sites in the crystal structure for $\text{Mg}(\text{BH}_4)_2(\text{NH}_3\text{BH}_3)_2$ (Table S1, Supporting Information). Using this assignment, and assuming that the experimental quadrupole tensor elements (Q_{ii}^{exp}) exhibit the same sign as the calculated V_{ii}^{calc} elements, results in the plot of Q_{ii}^{exp} as a function of the V_{ii}^{calc} elements after the DFT optimization of the $\text{Mg}(\text{BH}_4)_2(\text{NH}_3\text{BH}_3)_2$ structure shown in Figure 7. This plot shows a convincing correlation between the experimental and calculated tensor elements and linear regression analysis of the data gives the equation

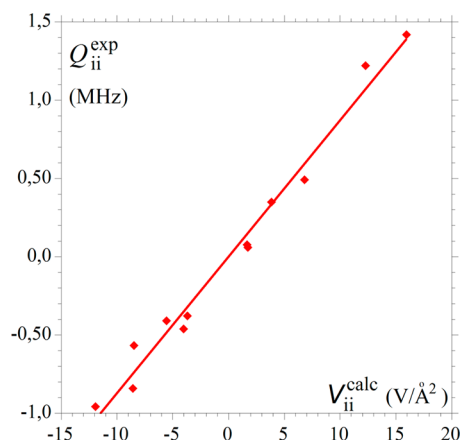


Figure 7. Correlation between the principal ^{11}B quadrupole coupling tensor elements (Q_{ii}^{exp}) and the corresponding calculated EFG tensor elements (V_{ii}^{calc}) from the DFT optimization of the SR-PXD structure of $\text{Mg}(\text{BH}_4)_2(\text{NH}_3\text{BH}_3)_2$. The calculated EFG tensor elements are summarized in Table 3. Linear regression analysis of the data is given in eq 4

$$Q_{ii}^{\text{exp}}(\text{MHz}) = 0.0872(\text{MHz}/(\text{V}\cdot\text{\AA}^{-2}))V_{ii}^{\text{calc}}(\text{V}\cdot\text{\AA}^{-2}) - 7.3 \times 10^{-6}(\text{MHz}) \quad (4)$$

with the correlation coefficient $R = 0.991$. A similar analysis of the Q_{ii}^{exp} data as a function of V_{ii}^{calc} elements before the DFT optimization (i.e., the PXD data in Table 3) results in the equation

$$Q_{ii}^{\text{exp}}(\text{MHz}) = 0.0831(\text{MHz}/(\text{V}\cdot\text{\AA}^{-2}))V_{ii}^{\text{calc}}(\text{V}\cdot\text{\AA}^{-2}) - 4.7 \times 10^{-9}(\text{MHz}) \quad (5)$$

and the correlation coefficient $R = 0.987$. Thus, a slightly improved agreement is observed between the experimental quadrupole tensor elements and those calculated after the DFT optimization of the structure. The largest difference between the two sets of calculated ^{11}B EFG data and their correlation with the experimental data are observed for the two ammonia

borane sites, in particular B(13), as evidenced by the calculated C_Q and η_Q values in Table 3. For the B(13) site, the asymmetry parameter changes from $\eta_Q^{\text{calc}} = 0.72$ to $\eta_Q^{\text{calc}} = 0.50$ after the DFT optimization, where the latter value is much closer to the experimental value of $\eta_Q = 0.35$. For the B(21) site the two calculated asymmetry parameters ($\eta_Q^{\text{calc}} = 0.34$ and 0.40) agree well with the experimental value (0.38) whereas C_Q changes from 1.34 to 1.24 MHz upon the DFT optimization, where the latter value is in full agreement with the experiment value, $C_Q = 1.221 \pm 0.025$ MHz. Thus, the comparison of the ^{11}B NMR data with the EFG tensor elements (Tables 2 and 3) indicates that crystal structure data may give a slightly improved representation of the crystal structure as compared to the SR-PXD structure data (Table S1, Supporting Information), principally for the local environments of the two ammonia borane sites. Finally, it is noted that the slopes of the linear correlations in eqs 4 and 5 correspond to ^{11}B nuclear quadrupole moments of $Q = 0.0361$ barn (after DFT optimization) and $Q = 0.0344$ barn (SR-PXD structure). These values are slightly smaller than the value $Q = 0.0409$ barn,⁵⁵ determined in an earlier ^{11}B NMR–DFT study of inorganic borates, and the value $Q = 0.0406$ barn,^{56,57} reported in recent compilations of nuclear quadrupole coupling moments.

3.5. Thermal Analysis. TGA-MS data are obtained for $\text{Mg}(\text{BH}_4)_2(\text{NH}_3\text{BH}_3)_2$ (s2) from room temperature to 400 °C (2 deg/min) and presented in Figure 8. TGA reveals a mass loss of 27 wt % between room temperature and 125 °C and an additional mass loss of 10 wt % in the temperature range from 125 to 400 °C. The differentiated TGA data (dTGA) indicate that a two-step reaction is taking place between room temperature and 125 °C. From the MS signals a mixture of hydrogen, ammonia, and a small amount of diborane and borazine are observed below 150 °C, while only hydrogen is observed above 150 °C. The TGA signal is remarkably different from those observed for both pristine NH_3BH_3 and α - $\text{Mg}(\text{BH}_4)_2$. NH_3BH_3 decomposes in two distinct steps between 100 and 175 °C,¹⁹ while pristine $\text{Mg}(\text{BH}_4)_2$ decomposes at ~ 365 °C.^{14,15} The TGA/DSC data measured for γ - $\text{Mg}(\text{BH}_4)_2$ –

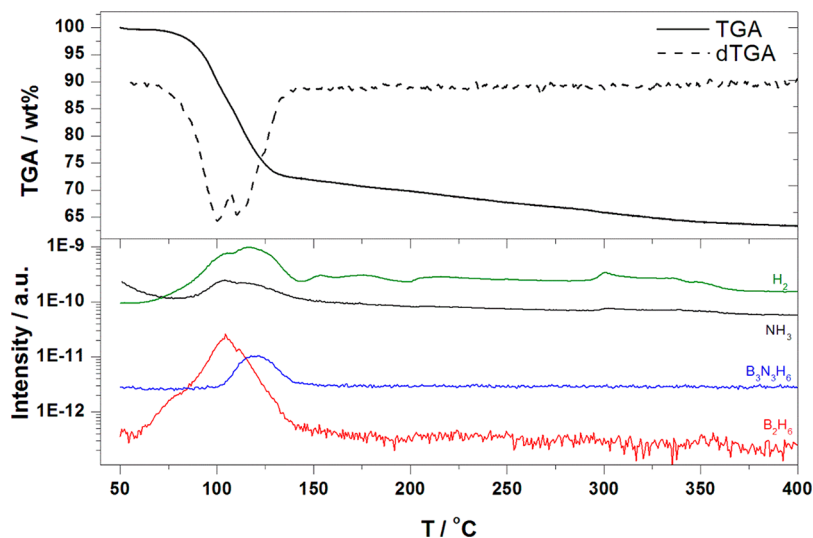


Figure 8. TGA-MS curves for $\text{Mg}(\text{BH}_4)_2(\text{NH}_3\text{BH}_3)_2$ (s2) heated from room temperature to 400 °C (2 °C/min). Upper part: The TGA data and dTGA are presented by a solid and dashed black line, respectively. Lower part: Corresponding MS signals shown for hydrogen, ammonia, borazine, and diborane presented by green, purple, red, and blue lines, respectively.

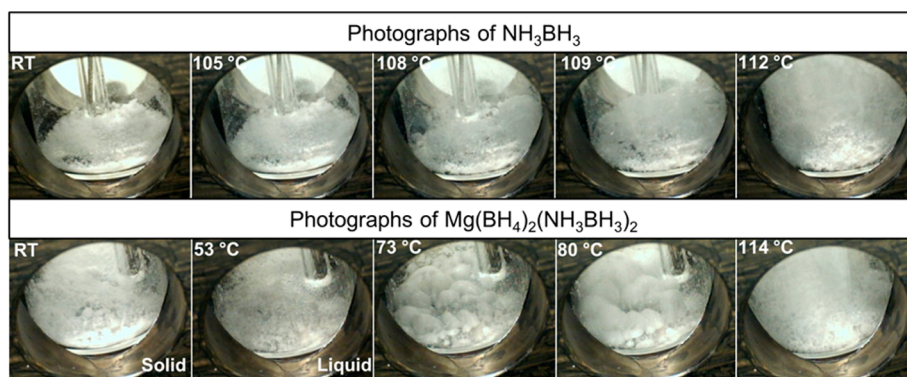


Figure 9. Temperature-programmed photographic analysis of NH_3BH_3 (upper row) and $\text{Mg}(\text{BH}_4)_2(\text{NH}_3\text{BH}_3)_2$ (lower row) heated from room temperature to 200 °C with a heating rate 4 deg/min in argon atmosphere.

NH_3BH_3 (1:2, s7) from room temperature to 500 °C (5 deg/min) are shown in Figure S16 (Supporting Information). This sample contains some unreacted NH_3BH_3 and amorphous $\text{Mg}(\text{BH}_4)_2$, as described previously, and the TGA data (Figure S16, Supporting Information) reveal a two- or three-step decomposition from 80 to 170 °C as a result of the presence of NH_3BH_3 . The DSC data reveal endothermic peaks at 48 and 85 °C and a strong exothermic peak at 100 °C. The two events at 85 and 100 °C cannot be clearly examined due to the presence of both NH_3BH_3 and $\text{Mg}(\text{BH}_4)_2(\text{NH}_3\text{BH}_3)_2$. However, the endothermic peak at 48 °C is described as the melting point of $\text{Mg}(\text{BH}_4)_2(\text{NH}_3\text{BH}_3)_2$, which is significantly lower than the melting point for NH_3BH_3 (100–114 °C).¹⁹

To confirm the melting point of $\text{Mg}(\text{BH}_4)_2(\text{NH}_3\text{BH}_3)_2$, a series of photographs of the powder of $\text{Mg}(\text{BH}_4)_2(\text{NH}_3\text{BH}_3)_2$ were collected between room temperature and 200 °C and compared with those of NH_3BH_3 (Figure 9). As expected, no changes are observed for the powder of NH_3BH_3 between room temperature and 100 °C, while the powder expands significantly in the temperature range from 108 to 112 °C, as previously reported.¹⁹ In contrast, $\text{Mg}(\text{BH}_4)_2(\text{NH}_3\text{BH}_3)_2$ melts and at 53 °C the powder is liquified. Above the melting point the sample starts to foam and at 70 °C it starts to expand slowly. When temperatures around 110 °C are reached, it expands significantly faster similar to the observations for pristine NH_3BH_3 . A fraction of $\text{Mg}(\text{BH}_4)_2(\text{NH}_3\text{BH}_3)_2$ was heated to 55 °C in argon atmosphere, cooled to room temperature, and characterized by PXD (Figure S17, Supporting Information). It is clearly revealed that the crystal structure of $\text{Mg}(\text{BH}_4)_2(\text{NH}_3\text{BH}_3)_2$ is remained, confirming that it is a melt.

In situ SR-PXD diffractograms (Figure S18, Supporting Information) have been obtained for the sample $\gamma\text{-Mg}(\text{BH}_4)_2\text{-NH}_3\text{BH}_3$ (1:0.66, s6) heated from room temperature to 88 °C (10 deg/min). These data reveal that all diffraction peaks from $\text{Mg}(\text{BH}_4)_2(\text{NH}_3\text{BH}_3)_2$ disappear at $T = 45$ °C and no new peaks appear, confirming the melting state. The activation energy for hydrogen release from $\text{Mg}(\text{BH}_4)_2(\text{NH}_3\text{BH}_3)_2$ was calculated in a previous study.³⁶ However, in that work they are not aware of the fact that $\text{Mg}(\text{BH}_4)_2(\text{NH}_3\text{BH}_3)_2$ decomposes from a melt, which then may lead to an inaccurate value for the activation energy.

3.6. Variable-Temperature ^{11}B MAS NMR. Variable-temperature (VT) ^{11}B MAS NMR spectra of the central transition region for $\text{Mg}(\text{BH}_4)_2(\text{NH}_3\text{BH}_3)_2$ following a stepwise heating of the sample from 3.9 to 73.1 °C is shown

in Figure 10. The spectra acquired at 3.9 and 33.2 °C resemble closely the spectrum in Figure 4a, thereby reflecting the presence of two well-defined NH_3BH_3 and two BH_4^- sites. At 40 °C the overlapping quadrupolar line shapes from the NH_3BH_3 sites become broader and intensity from the low-frequency BH_4^- site converts partly into a centerband at -39.5 ppm. The broadening of the quadrupolar line shapes reflects the formation of a new NH_3BH_3 site with a chemical shift shifted to higher frequency, as apparent from the spectrum recorded at 45.6 °C. At 48.2 °C the quadrupolar line shapes from the two distinct NH_3BH_3 sites have transformed into this new NH_3BH_3 environment, corresponding to the almost symmetric and rather narrow centerband with a center of gravity at $\delta_{\text{cg}} = -22.7$ ppm. The decrease in line width of this centerband may reflect that the new NH_3BH_3 site is influenced by motional processes that partially average out the quadrupole interaction. A similar resonance at -22.5 ppm has been observed in VT- ^{11}B MAS NMR spectra following the dehydrogenation of NH_3BH_3 at 88 °C and assigned to a new NH_3BH_3 phase.¹⁸ A structural change is also observed for the two distinct centerbands from the BH_4^- sites which at 48.2 °C have merged into a narrow resonance at $\delta_{\text{cg}} = -38.9$ ppm. These changes for the NH_3BH_3 and BH_4^- sites may reflect that the increase in temperature reduces the hydrogen bonding network, thereby allowing a higher degree of motion of the structural units, resulting in averaging of the quadrupole interactions for these sites. The rather narrow resonances and symmetric line shapes observed at 62.4 °C indicate a nearly complete averaging of the ^{11}B quadrupole interactions in accordance with the presence of a melt phase with a high viscosity. A further increase in temperature leads to a decrease in the intensity for the NH_3BH_3 site that is almost absent at 73.1 °C. Moreover, a minor fraction of a new type of boron species is observed at 62.4 and 68.6 °C by the presence of a centerband at $\delta_{\text{cg}} = -11.7$ ppm. This resonance may arise from $-\text{BH}_2$ sites,²⁰ and it broadens significantly at 73.1 °C where the spectrum otherwise only includes the resonance from the BH_4^- units. The centerband from the latter species shifts slightly to higher frequency on going from 68.6 to 73.1 °C ($\delta_{\text{cg}} = -38.2$ ppm). The main change observed in the VT ^{11}B MAS NMR spectra from 40.3 to 48.2 °C is in accord with the endothermic peak at 48 °C in the DSC experiment and reflects the breakdown of the $\text{Mg}(\text{BH}_4)_2(\text{NH}_3\text{BH}_3)_2$ structure. Moreover, the overall decrease in the ^{11}B centerband intensity on going from 48.2 to 73.1 °C, in particular for the $(\text{NH}_3\text{BH}_3)_2$ sites,

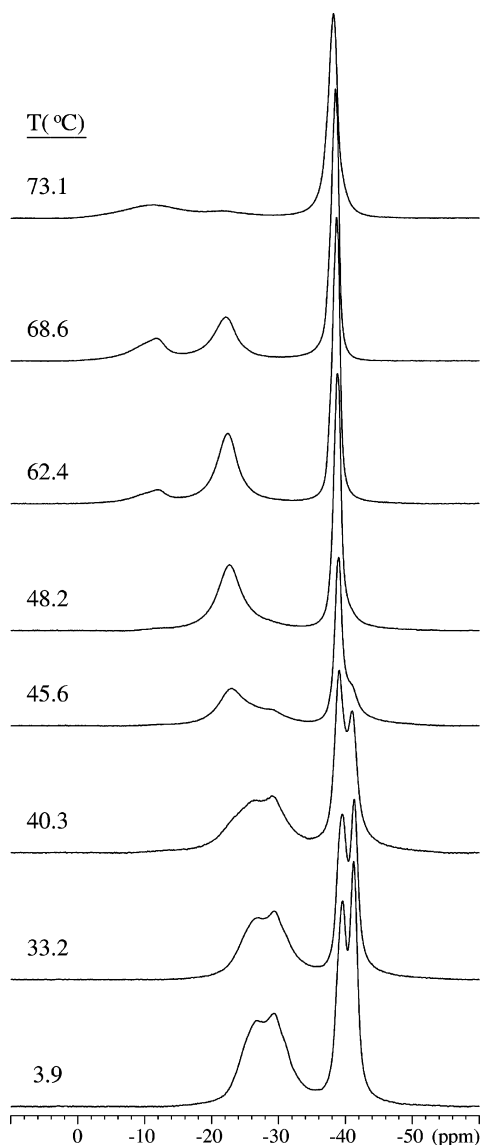


Figure 10. Variable-temperature ^{11}B MAS NMR spectra (7.05 T, $\nu_{\text{R}} = 6.0$ kHz) of the central transitions for $\text{Mg}(\text{BH}_4)_2(\text{NH}_3\text{BH}_3)_2$ (s2) following the decomposition with increasing temperature from 3.9 to 73.1 $^\circ\text{C}$.

agrees well with a release of boron-containing gases as indicated by the TGA-MS measurements.

3.7. Ex Situ PXD, ^{11}B MAS NMR, and FTIR. Fractions of $\alpha\text{-Mg}(\text{BH}_4)_2$, NH_3BH_3 , and $\text{Mg}(\text{BH}_4)_2(\text{NH}_3\text{BH}_3)_2$ (s2) were heated to 220 $^\circ\text{C}$ and naturally cooled to room temperature. Subsequently, these samples were characterized by PXD (Figure S19, Supporting Information), FTIR (Figure 11), and ^{11}B solid-state NMR (Figure 12).

PXD (Figure S19, Supporting Information) of $\text{Mg}(\text{BH}_4)_2(\text{NH}_3\text{BH}_3)_2$ heated to 220 $^\circ\text{C}$ and cooled to room temperature reveals reflections from $\alpha\text{-Mg}(\text{BH}_4)_2$ and the high temperature polymorph $\beta'\text{-Mg}(\text{BH}_4)_2$. Additionally, a small increase in the background is observed from 16 $^\circ$ to 22 $^\circ$, indicating the presence of an amorphous compound. FTIR of $\text{Mg}(\text{BH}_4)_2(\text{NH}_3\text{BH}_3)_2$ at room temperature reveals two bands in the N–H region with peak frequencies at 3307 and 3250 cm^{-1} and several bands in the B–H region with frequencies at 2471, 2397, 2299, 2247, and 2182 cm^{-1} (Figure 11 and Table S5, Supporting Information). These frequencies are comparable

with those observed for pure NH_3BH_3 and $\alpha\text{-Mg}(\text{BH}_4)_2$, as shown in Figure S20 (Supporting Information).⁵⁰ FTIR reveals one stretch in the N–H region at 3440 cm^{-1} for s2_220 and two stretches in the B–H region at 2494 and 2274 cm^{-1} . The Mg_220 sample shows bands similar to $\alpha\text{-Mg}(\text{BH}_4)_2$, while NH_3BH_3 _220 reveals the B–H (2494 cm^{-1}) and N–H (3440 cm^{-1}) stretches, which are the characteristic bands from polyimidoborane, $[\text{NHBH}]_n$.³⁷ It is clearly seen that the data for s2_220 can be considered as a sum of s2_220 and NH_3BH_3 _220, revealing that the products present at 220 $^\circ\text{C}$ are $\text{Mg}(\text{BH}_4)_2$ and $[\text{NHBH}]_n$. This is confirmed by a ^{11}B MAS NMR spectrum of Mg_220, (Figure 12) that includes a partly resolved second-order quadrupolar line shape from $[\text{NHBH}]_n$ ($\delta_{\text{cg}} = 22.8$ ppm) and a narrow resonance at -40 ppm from the BH_4^- sites in $\text{Mg}(\text{BH}_4)_2$. The quadrupolar line shape is in accordance with the parameters $\delta_{\text{iso}} = 30.1$ ppm, $C_{\text{Q}} = 2.91$ MHz, and $\eta_{\text{Q}} = 0.17$, determined for $[\text{NHBH}]_n$ from a ^{11}B MAS NMR spectrum obtained at lower magnetic field (7.05 T).³⁷ An evaluation of the centerband intensities gives a molar ratio of 0.44:1.0 between the ^{11}B sites in $[\text{NHBH}]_n$ and $\text{Mg}(\text{BH}_4)_2$.

3.8. Discussion. To summarize the thermal decomposition, $\text{Mg}(\text{BH}_4)_2(\text{NH}_3\text{BH}_3)_2$ melts at ~ 48 $^\circ\text{C}$ followed by decomposition in the temperature range 75 to 125 $^\circ\text{C}$ releasing a gas mixture of H_2 , NH_3 , B_2H_6 , and $\text{B}_3\text{N}_3\text{H}_6$. Hydrogen (10 wt %) is slowly released in the temperature range from 125 to 400 $^\circ\text{C}$, and α - and β' - $\text{Mg}(\text{BH}_4)_2$ as well as $[\text{NHBH}]_n$ are present in the sample at 220 $^\circ\text{C}$. The melting point at ~ 48 $^\circ\text{C}$ is on the one hand lower than the melting point for NH_3BH_3 (~ 112 $^\circ\text{C}$), but is on the other hand remarkably higher than melting points for molecular metal borohydrides such as $\text{Al}(\text{BH}_4)_3$ (< 0 $^\circ\text{C}$). This is explained by the strong dihydrogen bonds revealed by the DFT-optimized structural model. The thermal decomposition of $\text{Mg}(\text{BH}_4)_2(\text{NH}_3\text{BH}_3)_2$ is different from the previously reported $\text{M}(\text{BH}_4)_n\text{-NH}_3\text{BH}_3$ ($\text{M} = \text{Li}, \text{Na}, \text{K}, \text{or Ca}$) systems. For the system $\text{MBH}_4\text{-}2\text{NH}_3\text{BH}_3$ ($\text{M} = \text{Na}, \text{K}$), NH_3BH_3 decomposes independently of the presence of the metal borohydride, while $\text{LiBH}_4(\text{NH}_3\text{BH}_3)_{0.5}$ and $\text{Ca}(\text{BH}_4)_2(\text{NH}_3\text{BH}_3)_2$ decompose in steps similar to those for the individual components, i.e., first decomposition of NH_3BH_3 and at higher temperatures decomposition of the metal borohydrides.³⁴ The difference is explained by the different crystal structures for $\text{LiBH}_4\text{NH}_3\text{BH}_3$, $\text{LiBH}_4(\text{NH}_3\text{BH}_3)_{0.5}$, $\text{Ca}(\text{BH}_4)_2(\text{NH}_3\text{BH}_3)_2$, and $\text{Mg}(\text{BH}_4)_2(\text{NH}_3\text{BH}_3)_2$. $\text{Mg}(\text{BH}_4)_2(\text{NH}_3\text{BH}_3)_2$ is the only compound that melts, most likely as a result of the presence of molecular complexes of $\text{Mg}(\text{BH}_4)_2(\text{NH}_3\text{BH}_3)_2$ formed by Mg coordination to both BH_4^- and NH_3BH_3 groups as terminal ligands.

For the systems $\text{M}(\text{BH}_4)_n\text{-NH}_3\text{BH}_3$ ($\text{M} = \text{Li}, \text{Na}, \text{K}, \text{Mg}$ or Ca), NaBH_4 and KBH_4 are the only metal borohydrides that do not react with NH_3BH_3 forming borohydride–ammonia borane complexes. This may be correlated with the decreased polarization power of the metal cations for MBH_4 ($\text{M} = \text{Na}, \text{K}$) as compared with those for $\text{M}(\text{BH}_4)_n$ ($\text{M} = \text{Li}, \text{Mg}, \text{Ca}$). To investigate this further, $\text{RbBH}_4\text{-NH}_3\text{BH}_3$ (1:2) and $\text{CsBH}_4\text{-NH}_3\text{BH}_3$ (1:2) were treated mechanochemically and subsequently characterized by PXD (Figure S21, Supporting Information). The PXD data reveal for both samples that all diffraction peaks can be assigned to the starting materials, NH_3BH_3 and RbBH_4 or CsBH_4 . This shows that the $\text{RbBH}_4\text{-NH}_3\text{BH}_3$ (1:2) and $\text{CsBH}_4\text{-NH}_3\text{BH}_3$ (1:2) systems do not react during mechanochemical treatment similar to $\text{NaBH}_4\text{-NH}_3\text{BH}_3$ (1:2) or $\text{KBH}_4\text{-NH}_3\text{BH}_3$ (1:2), as expected

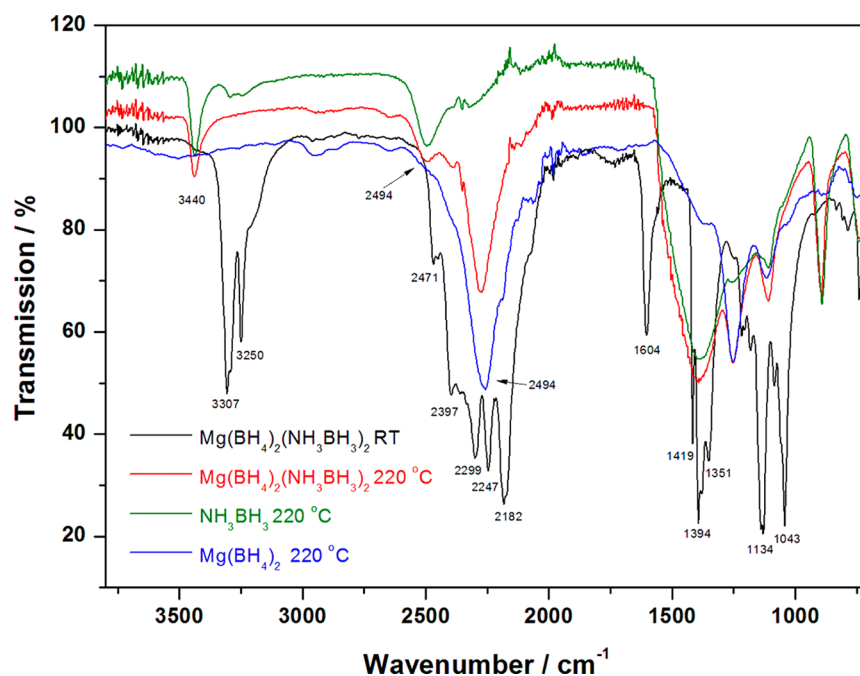


Figure 11. FTIR spectra recorded for $\text{Mg}(\text{BH}_4)_2(\text{NH}_3\text{BH}_3)_2$ at room temperature (black) and $\text{Mg}(\text{BH}_4)_2(\text{NH}_3\text{BH}_3)_2$, NH_3BH_3 , and $\text{Mg}(\text{BH}_4)_2$ heated to 220 °C presented by red, green, and blue lines, respectively.

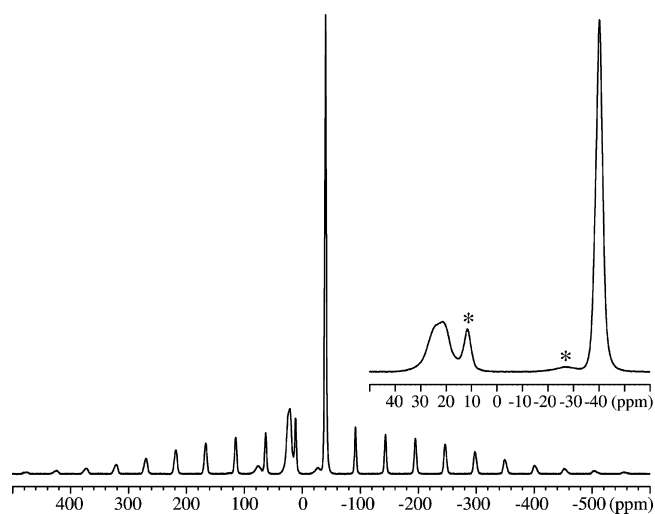


Figure 12. ^{11}B MAS NMR spectrum of $\text{Mg}(\text{BH}_4)_2(\text{NH}_3\text{BH}_3)_2$ heated to 220 °C (s2_220) and acquired at 14.09 T, using a spinning speed of $\nu_R = 10.0$ kHz. The inset shows the region for the central transitions where asterisks denote spinning sidebands.

according to the decreased polarization power. A similar trend has recently been observed for the dehydrogenation effect of $\text{M}(\text{BH}_4)_n$ ($\text{M} = \text{Li}, \text{Na}, \text{Mg}, \text{Ca}$) on $\text{Al}(\text{BH}_4)_3 \cdot 6\text{NH}_3$.⁵⁸ In that study, an increased hydrogen purity and lowered decomposition temperature was found for $\text{Al}(\text{BH}_4)_3 \cdot 6\text{NH}_3$ as a function of increasing polarization power for the added metal borohydride.

The systems $\text{M}(\text{BH}_4)_n\text{--NH}_3\text{BH}_3$ ($\text{M} = \text{Li}, \text{Na}, \text{K}, \text{Mg}, \text{Ca}$) have in common that they do not suppress the release of the toxic gases, e.g., B_2H_6 and $\text{B}_3\text{N}_3\text{H}_6$, as observed for metal amidoboranes.^{29,34–36} Thus, it may be concluded that the bonding of NH_3BH_3 is insufficiently modified for $\text{MBH}_4\text{--NH}_3\text{BH}_3$ ($\text{M} = \text{Li}, \text{Na}, \text{K}, \text{Mg}, \text{Ca}$), because NH_3BH_3 maintains its molecular form.^{24,34} This is in contrast to metal

amidoboranes where a metal is substituted for a hydrogen atom. Thus, the lack of pure hydrogen release from $\text{MBH}_4\text{--NH}_3\text{BH}_3$ systems must be addressed to utilize borohydride–ammonia borane systems for hydrogen storage in the future. Several attempts to achieve this goal may be possible, e.g., nanoconfinement, the addition of catalysts or by development of composite systems including metal hydrides such as $\text{Mg}(\text{BH}_4)_2(\text{NH}_3\text{BH}_3)_2\text{--LiH}$ or $\text{Mg}(\text{BH}_4)_2(\text{NH}_3\text{BH}_3)_2\text{--MgH}_2$, which all have been successful treatments for NH_3BH_3 .^{59,60}

4. CONCLUSION

In summary, $\text{Mg}(\text{BH}_4)_2(\text{NH}_3\text{BH}_3)_2$ has been mechanochemically synthesized from α - or γ - $\text{Mg}(\text{BH}_4)_2\text{--NH}_3\text{BH}_3$ (1:2). The crystal structure has been solved from SR-PXD data and subsequently confirmed by DFT calculations. ^{11}B quadrupole coupling parameters and isotropic chemical shifts have been determined with high precision for the two ammonia borane sites and the two borohydride sites from ^{11}B MAS NMR of the central and satellite transitions, respectively, and from ^{11}B MQMAS NMR. The quadrupole coupling parameters have been compared with ^{11}B electric field gradient tensor elements, obtained by DFT calculations, and thereby used to validate the crystal structures from SR-PXD and the subsequent DFT optimization. This comparison reveals that the structure gives the best agreement with the ^{11}B NMR data, most likely reflecting an improved description of the local environments for the two ammonia borane sites. The strong intermolecular dihydrogen bonds revealed by the optimized structural model may explain the relatively high melting point, 48 °C, for $\text{Mg}(\text{BH}_4)_2(\text{NH}_3\text{BH}_3)_2$ as compared to those for other molecular metal borohydrides. $\text{Mg}(\text{BH}_4)_2(\text{NH}_3\text{BH}_3)_2$ has a high gravimetric and volumetric H_2 content ($\rho_m = 17.4$ wt % H_2 , $\rho_v = 137$ g H_2/L), which makes it a good candidate for a new hydrogen storage material. Furthermore, $\text{Mg}(\text{BH}_4)_2(\text{NH}_3\text{BH}_3)_2$ has an attractive decomposition temperature for practical use, but suffers from the lack of pure

hydrogen release, which needs to be addressed in future work. Metal hydrides with low melting points are of interest for safe, fast, and efficient handling, e.g., refueling.

■ ASSOCIATED CONTENT

Supporting Information

Atomic coordinates and bond lengths in $\text{Mg}(\text{BH}_4)_2(\text{NH}_3\text{BH}_3)_2$, Rietveld refinement plots, and supporting PXD, FTIR and ^{11}B NMR data. This material is available free of charge via the Internet at <http://pubs.acs.org>.

■ AUTHOR INFORMATION

Notes

The authors declare no competing financial interest.

■ ACKNOWLEDGMENTS

The Danish Council for Strategic Research is acknowledged for financial support to project HyFillFast. The Danish National Research Foundation is thanked for funding to the Center for Materials Crystallography (DNRF93), the EU COST Action MP1103 and the Sino-Danish Center for Education and Research (SDC). The authors would like to thank Fonds National de la Recherche Scientifique, Belgium for the financial support and the fellowship to V.B. We are also grateful to the beamline ID15 and the Swiss-Norwegian Beamline at the ESRF, Grenoble and I11 at Diamond, Oxford for the provision of beam time. Especially, we are grateful to Agnieszka Poulain at ID15 for valuable help during our beam time. Finally, the use of the facilities at the Instrument Centre for Solid-State NMR Spectroscopy, Aarhus University, sponsored by the Danish Natural Science Research Councils and the Carlsberg Foundation, is acknowledged.

■ REFERENCES

- (1) Felderhoff, M.; Weidenthaler, C.; von Helmolt, R.; Eberle, U. Hydrogen Storage: The Remaining Scientific and Technological Challenges. *Phys. Chem. Chem. Phys.* **2007**, *9*, 2643–2653.
- (2) Schlapbach, L.; Züttel, A. Hydrogen-Storage Materials for Mobile Applications. *Nature* **2001**, *414*, 353–358.
- (3) Rude, L. H.; Nielsen, T. K.; Ravnsbæk, D. B.; Bösenberg, U.; Ley, M. B.; Richter, B.; Arnbjerg, L. M.; Dornheim, M.; Filinchuk, Y.; Besenbacher, F.; et al. Tailoring Properties of Borohydrides for Hydrogen Storage: A Review. *Phys. Status Solidi* **2011**, *208*, 1754–1773.
- (4) Schüth, F.; Bogdanović, B.; Felderhoff, M. Light Metal Hydrides and Complex Hydrides for Hydrogen Storage. *Chem. Commun.* **2004**, 2249–2258.
- (5) Orimo, S. I.; Nakamori, Y.; Eliseo, J. R.; Züttel, A.; Jensen, C. M. Complex Hydrides for Hydrogen Storage. *Chem. Rev.* **2007**, *107*, 4111–4132.
- (6) Chen, P.; Zhu, M. Recent Progress in Hydrogen Storage. *Mater. Today* **2008**, *11*, 36–43.
- (7) Huang, Z.; Autrey, T. Boron–nitrogen–hydrogen (BNH) Compounds: Recent Developments in Hydrogen Storage, Applications in Hydrogenation and Catalysis, and New Syntheses. *Energy Environ. Sci.* **2012**, *5*, 9257–9268.
- (8) Jepsen, L. H.; Ley, M. B.; Lee, Y.-S.; Cho, Y. W.; Dornheim, M.; Jensen, J. O.; Filinchuk, Y.; Jørgensen, J. E.; Besenbacher, F.; Jensen, T. R. Boron–nitrogen Based Hydrides and Reactive Composites for Hydrogen Storage. *Mater. Today* **2014**, *17*, 129–135.
- (9) Wiberg, E.; Bauer, R. Zur Kenntnis eines Magnesium-Bor-Wasserstoffs $\text{Mg}(\text{BH}_4)_2$. *Z. Naturforsch., B* **1950**, *5*, 397–397.
- (10) Černý, R.; Filinchuk, Y.; Hagemann, H.; Yvon, K. Magnesium Borohydride: Synthesis and Crystal Structure. *Angew. Chem., Int. Ed.* **2007**, *46*, 5765–5767.

- (11) Her, J. H.; Stephens, P. W.; Gao, Y.; Soloveichik, G. L.; Rijssenbeek, J.; Andrus, M.; Zhao, J. C. Structure of Unsolvated Magnesium Borohydride $\text{Mg}(\text{BH}_4)_2$. *Acta Crystallogr., Sect. B* **2007**, *63*, 561–568.

- (12) Filinchuk, Y.; Richter, B.; Jensen, T. R.; Dmitriev, V.; Chernyshov, D.; Hagemann, H. Porous and Dense Magnesium Borohydride Frameworks: Synthesis, Stability, and Reversible Absorption of Guest Species. *Angew. Chem., Int. Ed.* **2011**, *50*, 11162–11166.

- (13) David, W. I. F.; Callear, S. K.; Jones, M. O.; Aeberhard, P. C.; Culligan, S. D.; Pohl, A. H.; Johnson, S. R.; Ryan, K. R.; Parker, J. E.; Edwards, P. P.; et al. The Structure, Thermal Properties and Phase Transformations of the Cubic Polymorph of Magnesium Tetrahydroborate. *Phys. Chem. Chem. Phys.* **2012**, *14*, 11800–11807.

- (14) Paskevicius, M.; Pitt, M. P.; Webb, C. J.; Sheppard, D. A.; Filso, U.; Gray, E. M.; Buckley, C. E. In-Situ X-Ray Diffraction Study of Gamma- $\text{Mg}(\text{BH}_4)_2$ Decomposition. *J. Phys. Chem. C* **2012**, *116*, 15231–15240.

- (15) Li, H.-W.; Kikuchi, K.; Nakamori, Y.; Ohba, N.; Miwa, K.; Towata, S.; Orimo, S. Dehydrogenating and Rehydrogenating Processes of Well-Crystallized $\text{Mg}(\text{BH}_4)_2$ Accompanying with Formation of Intermediate Compounds. *Acta Mater.* **2008**, *56*, 1342–1347.

- (16) Marder, T. B. Will We Soon Be Fueling Our Automobiles with Ammonia–Borane? *Angew. Chem., Int. Ed.* **2007**, *46*, 8116–8118.

- (17) Wolf, G.; Baumann, J.; Baitalow, F.; Hoffmann, F. P. Calorimetric Process Monitoring of Thermal Decomposition of B–N–H Compounds. *Thermochim. Acta* **2000**, *343*, 19–25.

- (18) Baitalow, F.; Baumann, J.; Wolf, G.; Jaenicke-Rößler, K.; Leitner, G. Thermal Decomposition of B–N–H Compounds Investigated by Using Combined Thermoanalytical Methods. *Thermochim. Acta* **2002**, *391*, 159–168.

- (19) Staubitz, A.; Robertson, A. P. M.; Manners, I. Ammonia-Borane and Related Compounds as Dihydrogen Sources. *Chem. Rev.* **2010**, *110*, 4079–4124.

- (20) Stowe, A. C.; Shaw, W. J.; Linehan, J. C.; Schmid, B.; Autrey, T. In Situ Solid State ^{11}B MAS-NMR Studies of the Thermal Decomposition of Ammonia Borane: Mechanistic Studies of the Hydrogen Release Pathways from a Solid State Hydrogen Storage Material. *Phys. Chem. Chem. Phys.* **2007**, *9*, 1831–1836.

- (21) Sutton, A. D.; Burrell, A. K.; Dixon, D. A.; Garner, E. B.; Gordon, J. C.; Nakagawa, T.; Ott, K. C.; Robinson, J. P.; Vasiliu, M. Regeneration of Ammonia Borane Spent Fuel by Direct Reaction with Hydrazine and Liquid Ammonia. *Science* **2011**, *331*, 1426–1429.

- (22) Xiong, Z.; Yong, C. K.; Wu, G.; Chen, P.; Shaw, W.; Karkamkar, A.; Autrey, T.; Jones, M. O.; Johnson, S. R.; Edwards, P. P.; et al. High-Capacity Hydrogen Storage in Lithium and Sodium Amidoboranes. *Nat. Mater.* **2008**, *7*, 138–141.

- (23) Spielmann, J.; Jansen, G.; Bandmann, H.; Harder, S. Calcium Amidoborane Hydrogen Storage Materials: Crystal Structures of Decomposition Products. *Angew. Chem., Int. Ed.* **2008**, *47*, 6290–6295.

- (24) Wu, H.; Zhou, W.; Yildirim, T. Alkali and Alkaline-Earth Metal Amidoboranes: Structure, Crystal Chemistry, and Hydrogen Storage Properties. *J. Am. Chem. Soc.* **2008**, *130*, 14834–14839.

- (25) Zhang, Q.; Tang, C.; Fang, C.; Fang, F.; Sun, D.; Ouyang, L.; Zhu, M. Synthesis, Crystal Structure, and Thermal Decomposition of Strontium Amidoborane. *J. Phys. Chem. C* **2010**, *114*, 1709–1714.

- (26) Genova, R. V.; Fijalkowski, K. J.; Budzianowski, A.; Grochala, W. Towards $\text{Y}(\text{NH}_2\text{BH}_3)_3$: Probing Hydrogen Storage Properties of $\text{YX}_3/\text{MNH}_2\text{BH}_3$ ($\text{X} = \text{F}, \text{Cl}; \text{M} = \text{Li}, \text{Na}$) and $\text{YH}_{x-3}/\text{NH}_3\text{BH}_3$ Composites. *J. Alloys Compd.* **2010**, *499*, 144–148.

- (27) Diyabalanage, H. V. K.; Nakagawa, T.; Shrestha, R. P.; Semelsberger, T. A.; Davis, B. L.; Scott, B. L.; Burrell, A. K.; David, W. I. F.; Ryan, K. R.; Jones, M. O.; et al. Potassium(I)-Amidotrihydroborate: Structure and Hydrogen Release. *J. Am. Chem. Soc.* **2010**, *132*, 11836–11837.

- (28) Kang, X.; Fang, Z.; Kong, L.; Cheng, H.; Yao, X.; Lu, G.; Wang, P. Ammonia Borane Destabilized by Lithium Hydride: An Advanced On-Board Hydrogen Storage Material. *Adv. Mater.* **2008**, *20*, 2756–2759.

- (29) Chua, Y. S.; Chen, P.; Wu, G.; Xiong, Z. Development of Amidoboranes for Hydrogen Storage. *Chem. Commun.* **2011**, 47, 5116–5129.
- (30) Fijalkowski, K. J.; Genova, R. V.; Filinchuk, Y.; Budzianowski, A.; Derzsi, M.; Jaroń, T.; Leszczyński, P. J.; Grochala, W. Na[Li(NH₂BH₃)₂] – the First Mixed-Cation Amidoborane with Unusual Crystal Structure. *Dalton Trans.* **2011**, 40, 4407.
- (31) Chua, Y. S.; Wu, G.; Xiong, Z.; He, T.; Chen, P. Calcium Amidoborane Ammoniate—Synthesis, Structure, and Hydrogen Storage Properties. *Chem. Mater.* **2009**, 21, 4899–4904.
- (32) Chua, Y. S.; Wu, G.; Xiong, Z.; Karkamkar, A.; Guo, J.; Jian, M.; Wong, M. W.; Autrey, T.; Chen, P. Synthesis, Structure and Dehydrogenation of Magnesium Amidoborane Monoammoniate. *Chem. Commun.* **2010**, 46, 5752.
- (33) Wu, C.; Wu, G.; Xiong, Z.; Han, X.; Chu, H.; He, T.; Chen, P. LiNH₂BH₃·NH₃BH₃: Structure and Hydrogen Storage Properties. *Chem. Mater.* **2010**, 22, 3–5.
- (34) Wu, H.; Zhou, W.; Pinkerton, F. E.; Meyer, M. S.; Srinivas, G.; Yildirim, T.; Udovic, T. J.; Rush, J. J. A New Family of Metal Borohydride Ammonia Borane Complexes: Synthesis, Structures, and Hydrogen Storage Properties. *J. Mater. Chem.* **2010**, 20, 6550.
- (35) Luo, J.; Wu, H.; Zhou, W.; Kang, X.; Fang, Z.; Wang, P. LiBH₄·NH₃BH₃: A New Lithium Borohydride Ammonia Borane Compound with a Novel Structure and Favorable Hydrogen Storage Properties. *Int. J. Hydrogen Energy* **2012**, 37, 10750–10757.
- (36) Chen, X.; Yuan, F.; Gu, Q.; Yu, X. Synthesis, Structures and Hydrogen Storage Properties of Two New H-Enriched Compounds: Mg(BH₄)₂(NH₃BH₃)₂ and Mg(BH₄)₂(NH₃)₂(NH₃BH₃). *Dalton Trans.* **2013**, 42, 14365–14368.
- (37) Jepsen, L. H.; Skibsted, J.; Jensen, T. R. Investigations of the Thermal Decomposition of MBH₄–2NH₃BH₃, M = Na, K. *J. Alloys Compd.* **2013**, 580, S287–291.
- (38) Zanella, P.; Crociani, L.; Masciocchi, N.; Giunchi, G. Facile High-Yield Synthesis of Pure, Crystalline Mg (BH₄)₂. *Inorg. Chem.* **2007**, 46, 9039–9041.
- (39) Altomare, A.; Burla, M. C.; Camalli, M.; Carrozzini, B.; Cascarano, G. L.; Giacovazzo, C.; Guagliardi, A.; Moliterni, A. G. G.; Polidori, G.; Rizzi, R. EXPO: A Program for Full Powder Pattern Decomposition and Crystal Structure Solution. *J. Appl. Crystallogr.* **1999**, 32, 339–340.
- (40) Favre-Nicolin, V.; Cerný, R. FOX, “Free Objects for Crystallography”: A Modular Approach to Ab Initio Structure Determination from Powder Diffraction. *J. Appl. Crystallogr.* **2002**, 35, 734–743.
- (41) Rodriguez-Carvajal, J. *Fullprof Suite*; LLB Sacley & LCSIM Rennes, France, 2003.
- (42) Spek, A. L. Structure Validation in Chemical Crystallography. *Acta Crystallogr., Sect. D* **2009**, 65, 148–155.
- (43) Kresse, G.; Furthmüller, J. Efficient Iterative Schemes for Ab Initio Total-Energy Calculations Using a Plane-Wave Basis Set. *Phys. Rev. B* **1996**, 54, 11169–11186.
- (44) Perdew, J. P.; Burke, K.; Ernzerhof, M. Generalized Gradient Approximation Made Simple. *Phys. Rev. Lett.* **1996**, 77, 3865–3868.
- (45) Blöchl, P. E. Projector Augmented-Wave Method. *Phys. Rev. B* **1994**, 50, 17953–17979.
- (46) Petrilli, H. M.; Blöchl, P. E.; Blaha, P.; Schwarz, K. Electric-Field-Gradient Calculations Using the Projector Augmented Wave Method. *Phys. Rev. B* **1998**, 57, 14690–14697.
- (47) Paskevicius, M.; Ley, M. B.; Sheppard, D. A.; Jensen, T. R.; Buckley, C. E. Eutectic Melting in Metal Borohydrides. *Phys. Chem. Chem. Phys.* **2013**, 15, 19774–19789.
- (48) Amoureux, J.-P.; Fernandez, C.; Steuernagel, S. Z-Filtering in MQMAS NMR. *J. Magn. Reson. A* **1996**, 123, 116–118.
- (49) Skibsted, J.; Nielsen, N. C.; Bildsøe, H.; Jakobsen, H. J. Satellite Transitions in MAS NMR Spectra of Quadrupolar Nuclei. *J. Magn. Reson.* **1991**, 95, 88–117.
- (50) Filinchuk, Y.; Černý, R.; Hagemann, H. Insight into Mg(BH₄)₂ with Synchrotron X-Ray Diffraction: Structure Revision, Crystal Chemistry, and Anomalous Thermal Expansion. *Chem. Mater.* **2009**, 21, 925–933.
- (51) Klooster, W. T.; Koetzle, T. F.; Siegbahn, P. E. M.; Richardson, T. B.; Crabtree, R. H. Study of the N-H Center Dot Center Dot Center Dot H-B Dihydrogen Bond Including the Crystal Structure of BH₃NH₃ by Neutron Diffraction. *J. Am. Chem. Soc.* **1999**, 121, 6337–6343.
- (52) Rude, L. H.; Corno, M.; Ugliengo, P.; Baricco, M.; Lee, Y.-S.; Cho, Y. W.; Besenbacher, F.; Overgaard, J.; Jensen, T. R. Synthesis and Structural Investigation of Zr(BH₄)₄. *J. Phys. Chem. C* **2012**, 116, 20239–20245.
- (53) Gennari, F. C.; Fernández Albanesi, L.; Rios, I. J. Synthesis and Thermal Stability of Zr(BH₄)₄ and Zr(BD₄)₄ Produced by Mechanochemical Processing. *Inorg. Chim. Acta* **2009**, 362, 3731–3737.
- (54) Aldridge, S.; Blake, A. J.; Downs, A. J.; Gould, R. O.; Parsons, S.; Pulham, C. R. Some Tetrahydroborate Derivatives of Aluminium: Crystal Structures of Dimethylaluminium Tetrahydroborate and the and Phases of Aluminium Tris (tetrahydroborate) at Low Temperature. *J. Chem. Soc., Dalton Trans.* **1997**, 1007–1012.
- (55) Hansen, M. R.; Madsen, G. K. H.; Jakobsen, H. J.; Skibsted, J. Refinement of Borate Structures from ¹¹B MAS NMR Spectroscopy and Density Functional Theory Calculations of ¹¹B Electric Field Gradients. *J. Phys. Chem. A* **2005**, 109, 1989–1997.
- (56) Sundholm, D.; Olsen, J. Large Multiconfiguration Hartree–Fock Calculations on the Hyperfine Structure of B(²P) and the Nuclear Quadrupole Moments of ¹⁰B and ¹¹B. *J. Chem. Phys.* **1991**, 94, 5051–5055.
- (57) Pyykko, P. The Nuclear-Quadrupole Moments of the 20th Elements-High-Precision Calculations on Atoms and Small Molecules. *Z. Naturforsch.* **1992**, 47, 189–196.
- (58) Tang, Z.; Tan, Y.; Wu, H.; Gu, Q.; Zhou, W.; Jensen, C. M.; Yu, X. Metal Cation-Promoted Hydrogen Generation in Activated Aluminium Borohydride Ammoniates. *Acta Mater.* **2013**, 61, 4787–4796.
- (59) He, T.; Xiong, Z.; Wu, G.; Chu, H.; Wu, C.; Zhang, T.; Chen, P. Nanosized Co- and Ni-Catalyzed Ammonia Borane for Hydrogen Storage. *Chem. Mater.* **2009**, 21, 2315–2318.
- (60) Gutowska, A.; Li, L.; Shin, Y.; Wang, C. M.; Li, X. S.; Linehan, J. C.; Smith, R. S.; Kay, B. D.; Schmid, B.; Shaw, W.; et al. Nanoscaffold Mediates Hydrogen Release and the Reactivity of Ammonia Borane. *Angew. Chem., Int. Ed.* **2005**, 44, 3578–3582.